University of Nevada Reno

Lidar-Derived Forest Metrics Are Critical for Predicting Snow Accumulation and Ablation in the Central Sierra Nevada, USA

A thesis submitted in partial fulfillment of the requirements for the degree of Master of Science in Hydrology

by
Cara R. Piske
Dr. Adrian A. Harpold/Thesis Advisor

August 2022

THE GRADUATE SCHOOL

We recommend that the thesis
prepared under our supervision by

entitled

be accepted in partial fulfillment of the
requirements for the degree of

Advisor

Committee Member

Committee Member

Graduate School Representative

David W. Zeh, Ph.D., Dean
Graduate School

Abstract

Snowmelt is a critical source of water resources for ecosystems and communities surrounding the Sierra Nevada. Forest canopy controls critical mass and energy balance dynamics that can alter snowpack accumulation and ablation. In addition to changing climate dynamics that could shift the precipitation regimes of this region, an increase in ecosystem disturbance (e.g., drought, wildfires) creates dynamic forest structures that have the ability to drastically alter the snowpack. Forest management aims at creating resilient ecosystems but is often less explicitly focused on retaining the snowpack as a crucial water reservoir. It is important to constrain how fine-scale forest structures impact snowpack accumulation and persistence to predict future dynamics and inform management. However, while broad-scale forest structure metrics have been studied extensively in relation to snowpack, less is known about how fine-scale forest structure impacts snowpack. Light detection and ranging (lidar) data provide the opportunity to understand these complex dynamics using high resolution, spatially distributed points that capture detailed forest structure and snow depth. We use lidar collected over the course of multiple accumulation seasons both pre- and post-disturbance in Sagehen Creek Basin in the central Sierra Nevada to investigate how snowpack accumulation is impacted by fine-scale forest structure metrics, like leaf area index (LAI') and the ratio of gap width to average tree height (openness) in a 30-meter grid cell. In addition, we use a series of measurements taken during the ablation season to understand how forest structures impact snow persistence. Through developing a refined space-for-structure processing protocol, we show a delicate balance between the fraction of forest cover (fVEG) and openness in an area that promotes snowpack accumulation and reduces ablation. In general, areas with lower fVEG (0.3) and smaller gaps (diameter/height ~0.1)

increase accumulation. However, decreasing gap sizes and increasing fVEG can also lead to more ablation, supporting climate-driven paradigms that predict more ablation under the canopy in regions like the Sierra Nevada. Pre- and post-disturbance analyses show inconsistent patterns because of confounding accumulation and ablation dynamics at the date of collection. Our processing protocol and space-for-structure analysis provide a unique opportunity to understand lidar-derived forest-snow dynamics in a way that is transferrable to areas with varying vegetation and climate regimes.

Keywords: snow-hydrology, ecohydrology, forest disturbance, snow-vegetation

Acknowledgements

This endeavor would not have been possible without support from my thesis advisor, Dr. Adrian Harpold, who was integral to the development of my research questions and continually refined methodology, in addition to my committee members, Dr. Gabrielle Boisramé, Dr. Rosemary Carroll, and Dr. Alex Lutz who provided invaluable guidance ranging from fieldwork expertise to career support to feedback on analyses.

I would like to highlight our funding and data sources. Funding sources include the Nevada NASA Space Grant Consortium, the National Forest Service, and the Critical Zone Collaborative Network (CZCN) (EAR # 2012310 and 2012188 respectively). I would like to thank Dr. Julia Perdrial and Dr. Kristen Underwood, who brought science approaches back to impact focused, values-driven frameworks. Data sources include the National Center for Airborne Laser Mapping and the Airborne Snow Observatory. Dr. Kat Bormann and Dr. Joe Boardman provided both access to data and valuable feedback on our methodology.

Dr. Tiho Kostadinov both provided, data, code, and expertise. Dr. Justin Huntingon, Dr. Andrés Varhola, Dr. Kevin Shoemaker, Louis Graup provided data and code.

The Mountain Ecohydrology group, including Dr. Sebastian Krogh, Dr. Gabriel Lewis, Beatrice Gordon, Aidan Manning, Eli Boardman, Helena Middleton, Kate Miller, and Shaun Joseph, has supported me in countless ways. Marianna Webb is the reason I both came to UNR and have a home here. Our GPHS cohort formed necessary support systems and lifelong friendships (Ari Koshkin, Bri (and Mike) Hernandez, Darren Thomas, Drake McCrimmon, Hannah Van Dusen, Ian McDowell, James Phillips, Jack Tarricone, Lauren Bartels, Maddy Fontaine, Marc Berghouse (and parents), Sophie Rothman). Lastly, thank you to my family, partner (Jan Ketterson), and friends for endless love and support.

Table of Contents

List of Tables

List of Figures

List of Key Terms

Disturbance – A forcing large enough to cause a state change that impacts Critical Zone function. Importantly, in the context of the Sierra Nevada ecosystem, this term encompasses changes that occurred prior to Euro-American settlement (lightning ignited wildfire or indigenous burns) that reinforced resilience, changes that decrease resilience (high-intensity fires in overly dense forests), and changes due to management practices like thinning.

Resilience – socio-ecological systems' "…capacity to withstand and bounce back from disturbances and impacts, and—if necessary—to learn and transform themselves while continuing or regaining the ability to provide essential functions, services, amenities, or qualities…" (Moser et al., 2009).

SWE – snow water equivalent, or the amount of water held within a snowpack (measured in depth)

Critical Zone (CZ) – the region between the bedrock and treetops

1 Introduction

Around one sixth of the world's population relies on snowmelt-derived water resources (Barnett et al., 2005). Warming-induced climate trends predict a future of shifting climatic regimes resulting in increased precipitation variability (magnitude and form) and an overall decrease in snowpack accumulation and retention (Bales et al., 2006; Barnett et al., 2005; Huning & AghaKouchak, 2018; Li et al., 2017; Moser et al., 2009; North, 2012; Serreze et al., 1999). The western U.S. is particularly vulnerable to these shifting dynamics because it has historically relied on snow in the higher, wetter elevations to support its water resource needs (Barnhart et al., 2016; Godsey et al., 2014; Harpold et al., 2017; Musselman et al., 2015). The Sierra Nevada mountains sit within a snow-dominated precipitation regime and feed over half of California's water supply. Particularly in high-elevation systems, the snowpack serves as a natural water tower, driving evapotranspiration dynamics, dictating the timing of peak soil moisture, and sustaining low streamflow into the dry summer months (Barnhart et al., 2016; Cooper et al., 2020; Godsey et al., 2014; Hammond et al., 2019; Harpold, Molotch, et al., 2014; Li et al., 2017; Lundquist & Loheide, 2011).

Climate is the primary control on the broad-scale precipitation patterns that drive snowpack accumulation and energy flux patterns that dictate ablation; however, terrain and vegetation serve as secondary controls and can buffer or enhance climate impacts on water resources. In some locations, the spatial variability in snowpack distribution can be explained by terrain characteristics. High-elevation, steep, northern-facing slopes in the Sierra Nevada typically both accumulate and retain more snow (Godsey et al., 2014; Jost et al., 2007; Mazzotti et al., 2019; Tennant et al., 2017; Varhola et al., 2010).

Forest-snow interactions have been of historical interest in the Sierra Nevada. Records of field-based studies extend to the early 20th century, showing a delicate balance between accumulation and ablation. Vegetation influences energy fluxes that control snowpack retention, shading the snowpack from shortwave radiation and emitting longwave radiation. Shortwave radiation typically dominates ablation energy fluxes in the Sierra Nevada, but longwave radiation from forest canopy can be important when solar irradiance is low, which depends on seasonality, local climate, and terrain (Broxton et al., 2021; Dickerson-Lange et al., 2021; Hubbart et al., 2015; Kostadinov et al., 2019; Lundquist et al., 2013; Mazzotti et al., 2019; Safa et al., 2021; Zheng et al., 2019). In warmer regions, like the Sierra Nevada, with average winter temperatures ~-1°C and minimal wind redistribution, up to 60% of precipitation can be intercepted and sublimated from the forest (Harpold, Guo, et al., 2014; Hubbart et al., 2015; Safa et al., 2021; Schneider et al., 2019; Zheng et al., 2019). Moreover, the interplay between mass and energy fluxes in the Sierra Nevada, where ablation primarily occurs earlier in the spring when solar irradiance is low, suggest that snow will ablate more quickly and disappear earlier under forest canopy locations compared to the open areas due to the dominance of longwave radiation as an ablating force (over shortwave radiation) (Lundquist et al., 2013). Fine-scale accumulation and ablation patterns depend on tree-scale variability causing gaps (Lundquist et al., 2013; Safa et al., 2021), forest clumps, edges of different vegetation density, and height (Broxton et al., 2015; Hubbart et al., 2015; Russell et al., 2021; Tennant et al., 2017). While these fine-scale forest structure metrics exert strong controls on snowpack distribution, studies commonly focus on binary canopy-open classifications or broad scale, poorly defined canopy density metrics to investigate forest-snow interactions (Broxton et al., 2021; Harpold et al., 2020; Lundquist et al., 2013; Mazzotti

et al., 2019; Stevens, 2017; Varhola et al., 2010). Dynamic canopy conditions due to increased ecosystem disturbance (e.g., wildfire, beetle kill) add to the complexity of these processes.

A combination of climate change and fire suppression has resulted in dry, overly dense forests vulnerable to unprecedented high-intensity disturbance. Today, activate forest management attempts to return systems to more heterogeneous states, reminiscent of historical resilient conditions, by introducing low-moderate severity disturbances (e.g., prescribed wildfire, thinning). Wildfires, for example, historically sculpted a mosaic of forest structures that co-benefitted a myriad of processes throughout the Critical Zone (CZ) by maintaining and creating diverse vegetation types (e.g. shrubs, wetlands, forests). This led to an increase in streamflow and resulted in wetter soils due to the reduction of high-water use vegetation (e.g., Boisramé et al., 2019; Rakhmatulina et al., 2021; Stephens et al., 2021). In reference watersheds throughout the Sierra Nevada, efforts are underway to introduce low-moderate severity fires and selective thinning back into the landscape in order to create forest conditions that promote ecosystem function similar to historical conditions (North, 2012; Rakhmatulina et al., 2021; Stephens et al., 2021). These efforts are predicted to result in increasing hydrological outputs from impacted watersheds, including an increase in snowmelt magnitude (Boisramé et al., 2019; Stephens et al., 2021). However, tools to assess larger scale disturbance effects on snowpack accumulation and retention depend on specific vegetation structures, antecedent conditions, terrain, and the nature of the disturbance itself (Bart et al., 2021; Du et al., 2016; Ellis et al., 2013; Harpold et al., 2020; Jost et al., 2007; Krogh et al., 2020; Xu et al., 2018).

There is a knowledge gap regarding how vegetation (and vegetation disturbance) interacts with terrain to alter snowpack dynamics. Varhola et al. (2010), provides a good

example of the current paradigm, and showed through a meta-analysis of more than 30 studies that accumulation generally increased as the fraction of area covered by forests (fVEG) decreased, while ablation generally decreased as fVEG increased. However, their field-based method could not ascertain clear climate or terrain effects. Recent evidence shows that spatially distributed measurements can capture more nuanced vegetation impacts on snowpack than plot-scale field observations, highlighting that lower canopy is critical to radiation dynamics, edge effects are varied and can enhance or dampen vegetation-accumulation signals, and interception efficiency is both important and hard to capture (Currier & Lundquist, 2018; Mazzotti et al., 2020; Musselman et al., 2012; Russell et al., 2021; Safa et al., 2021; Webster et al., 2020). The methodological framework used by Varhola et al. (2010), combined many field-observations, compared snow water equivalent (SWE) at control sites (of varying scales) to reference sites (with either more or less vegetation) and remains a useful approach that could take advantage of new spatially distributed data.

Airborne light detection and ranging (lidar) has led to a data revolution that can help answer some of the biggest questions about spatial (and temporal) trends in snow processes under the forests (Broxton et al., 2015; Deems et al., 2013; Painter et al., 2016). Lidar offers substantial advantages over other remote sensing tools because emitted light pulses can penetrate gaps in vegetation and create a spatially distributed ground surface model at a sub-meter resolution and decimeter accuracy over extents greater than 100 km^2 (Deems et al., 2013; Hopkins et al., 2004; Krogh et al., 2020; Moeser et al., 2020; Painter et al., 2016). Previous studies have validated the reliability of lidar as a tool to capture under-forest snowpack but has generally focused on resolving snow depth or snow-covered area instead of SWE, which incorporates snow depth and density. SWE is more complicated to derive

and more valuable in terms of hydrologic understanding (Broxton et al., 2015; Deems et al., 2013; Harder et al., 2020; Hopkins et al., 2004; Hopkinson et al., 2010; P. B. Kirchner et al., 2014; Kostadinov et al., 2019; Mazzotti et al., 2019; Painter et al., 2016; Safa et al., 2021; Tinkham et al., 2014). There are few consistent processing methods to resolve SWE from lidar-derived snow depth in dense forests because, while lidar can penetrate gaps in vegetation, the number of returns is reduced due to interactions with vegetation, low branches can be confounded with the snow surface, and variable snow density adds spatial heterogeneity (both vertically throughout the snowpack and horizontally over the landscape). Moreover, large-scale processing of dense point clouds is computationally intensive and requires expert knowledge of vertical and lateral biases typical in these datasets (Deems et al., 2013; Kostadinov et al., 2019; Painter et al., 2016). Developing a consistent and open-source tool to estimate the effects of vegetation on SWE accumulation and ablation could improve our understanding of processes and provide simple tools to forest managers.

Taking advantage of a unique set of lidar datasets at Sagehen Creek Basin in the Sierra Nevada, California, we investigate how fine-scale forest structure metrics interact with terrain to control snowpack accumulation and retention. We follow the Varhola et al. (2010) reference-site framework to develop a "space-for-structure" (explained in more detail later) approach that estimates the bulk snow in a 30-m grid cell compared to reference (open or forested) 1-m pixels within that grid cell. Using this novel method for processing lidar datasets, we ask the following questions over the complex topography and heterogenous forest canopy of the >20 km^2 Sagehen Creek domain:

1. How does the fraction of vegetation in an area influence snow accumulation and ablation?

2. What role does terrain (elevation, aspect, and slope) play versus finer-scale vegetation structure (openness) on snow accumulation and ablation?
3. Does pre- and post-disturbance lidar imply similar changes in snow accumulation to the space-for-structure approach, and what management recommendations can be drawn from those relationships?

We combine the Varhola et al. (2010) approach with Random Forest (RF) modeling to answer the first two research questions and take advantage of three snow accumulation flights (2008, 2016, and 2022) and three flights over early and late-season ablation periods (March-April and April-May of 2016). We repeat these analyses, further refining the space-for-structure approach, post-thinning in 2022 to answer question 3. A primary goal was to create a replicable, open-source workflow to process point clouds, targeting snow and canopy metrics. In this way, our work serves as an important proof-of-concept for a new method to improve our understanding of snow-vegetation interactions and provide skillful estimates on the impacts of forest disturbance.

2 Methods

2.1 Study Site

Sagehen Creek Basin (SCB), located in the eastern Sierra Nevada, spans 28 km^2 and ~1800-2650 meters in elevation. Our study domain is ~7 by 8 km, extending beyond the watershed (Figure 1). The Basin has a unique record of research spanning 50+ years (J. Kirchner et al., 2005; Mast & Clow, 2000; North, 2012; *Sagehen Project*, 2013). SCB sits within the Sierran Steppe-Mixed Forest-Coniferous Forest-Alpine Meadow Province, and dominant vegetation types include Jeffrey Pine (*P. jeffreyi*), Lodgepole Pine (*Pinus contorta*), Ponderosa Pine (*P. ponderosa*), Red Fir (*A. magnifica*), Sugar Pine (*P. lambertiana*), Western White Pine (*P. monticola*), and White Fir (*Abies concolor*) (Mast & Clow, 2000). The Mediterranean climate in this region has warm, dry summers and cold, wet winters. Precipitation is dominated by snow (J. Kirchner et al., 2005; Mast & Clow, 2000; North, 2012; Trujillo & Molotch, 2014). There are three snow telemetry (SNOTEL) sites within or directly surrounding the basin, which measure depth and SWE using snow pillows. Median peak SWE ranges from 37 cm at the lowest SNOTEL site (Station Name: Independence Creek; Station ID: 540, Elevation 1961 m) to 113 cm at the highest site (Station Name: Independence Lake, Station ID: 541, Elevation 2541 m). The mean winter temperature is -1°C (Serreze et al., 1999).

The ecohydrology of SCB has been shaped by a complicated history of management – and mismanagement. Indigenous forest management (e.g., prescribed burns), primarily influenced by the presence of the Washoe (Wá·šiw) Tribe, promoted a heterogeneous ecosystem from ~1200 CE until the mid-19th century. Fire return intervals were around two years in the area during this time (Lindstom et al., 1999; Washoe Tribe, 2021). The onslaught of Euro-American settlement led to a period of timber harvesting until the early 20th century

and fire suppression thereafter when the U.S. Forest Service gained control over the watershed. This suppression resulted in dense, homogenous forests susceptible to high-intensity disturbance (e.g. wildfire, drought) (Moser et al., 2009; North, 2012; *Sagehen Project*, 2013; Vaillant & Stephens, 2009). The "Sagehen Fuels Reduction Project," a collaborative effort aimed at restoring and enhancing ecological heterogeneity and resilience to wildfires, has had a significant impact on the landscape of SCB. Fuel treatments, including prescribed burns and forest thinning, were implemented at target sites in the late 2010s (Figure 1). The goal of these management initiatives was to restore ecosystem function and enhance species conservation. However, less is known about how treatments, or landscape disturbances, explicitly influence hydrological processes driven by snowmelt. As the Sagehen Project is meant to represent management that could be applied elsewhere, it is integral that all elements of CZ response to disturbance are understood (Mast & Clow, 2000; North, 2012; *Sagehen Project*, 2013).

2.2 Lidar Data and Processing

Lidar is an active remote sensing tool that emits pulses of light at near infrared wavelengths (typically 1064 nm). At the target scales for this study (individual tree to hillslope), data is collected using airborne instruments. Emitted pulses are reflected off objects and the lidar scanner calculates a distance from the source based on the return time of the pulse. Lidar resolution is a function of points per square-meter (See Table A4 for resolution specifications of the data used in this study). Unlike other remote sensing tools which are limited to passive spectral reflectance signatures (like structure for motion) or are scattered by vegetation, lidar pulses can penetrate gaps in vegetation. While multiple returns can result in decreased return intensity, the instruments typically retrieve a high enough point

density (1.5-25 points/m^2) to resolve fine scale forest structure and the snowpack surface (Deems et al., 2013; Gatziolis & Andersen, 2008; Hopkins et al., 2004; Tinkham et al., 2014; Webster et al., 2020; Zheng et al., 2019).

A major limitation of lidar data is the temporal resolution, and the cost of acquisition can inhibit multiple flights. While April 1 SWE is typically assumed to represent peak SWE throughout the watershed, and targeted for lidar data acquisitions, SNOTEL data often reveal ablation at lower elevation sites (e.g., Figure 2). Therefore, early lidar flights can be valuable to investigate accumulation dynamics because ablation is less likely. However, climate variability complicates predicting the timing for peak SWE, and later flights can provide more useful information to stakeholders interested in the magnitude of spring melt, water reservoir managers, for example.

The study period was from 2008 to 2022, with specific dates of inquiry driven by data availability. Later flights were impacted by significant ablation, particularly at lower elevations (Figure 2). Despite their temporal limitations, these data present a unique opportunity in two ways. Firstly, a series of multi-temporal flights in 2016 captured both early and late season ablation, allowing us to take advantage of spatially distributed SWE data (as opposed to snow-covered-area data products provided by other remote sensing sources) to investigate ablation dynamics. Secondly, pre- and post-disturbance data allowed us to directly interrogate the impacts of specific forest management practices (thinning in 2017) on snowpack accumulation.

Lidar data was sourced from the Airborne Snow Observatory (ASO) and the National Center for Airborne Laser Mapping (NCALM). Snow depth was calculated by differencing snow-on and snow-off flights. Pre-disturbance, snow-off lidar was flown by NCALM in the

summer of 2014 with an average point density of 8.93 pts/m^2 (Guo, 2014). Pre-disturbance, snow-on lidar was flown in the early accumulation season of 2008 (on 02/10) by NCALM, with an average point density 4.9 pts/m^2 and again in 2016 by ASO at peak SWE (3/26), early in the ablation season (4/17), and late in the ablation season (5/18) with average point densities ~2 pts/m^2 (Dozier & Painter, 2004; Huntington, 2008). Post-disturbance, snow-off lidar was acquired by NCALM in the fall of 2020 (11/20) with an average point density of 20.98 pts/m^2 (Graup, 2021). Post-disturbance, snow-on lidar was also flown by NCALM. Though this flight was targeted to capture peak SWE in late March, early accumulation followed by a long period of ablation shifted the ablation season ~10 days (Figure 2). The data was ultimately collected in the spring of 2022 (3/21) with an average point density of 28 pts/m^2 (Piske, 2022).

Data processing was modified from the workflow of Kostadinov et al., 2019 (See Appendix A for more details on processing) to optimize reproducibility and to enable analyses in diverse vegetation types. The 2014 data were used for all terrain calculations and snow-off ground-truths both to maintain consistency, and because the 2020 flight was taken just after the first snowfall. While the 2020 data contains minimal snow accumulation, we used the 2014 flight to be conservative. The height above ground can be determined using a point to pixel subtraction, with the 2014 digital elevation model (DEM) as the ground reference. Vertical bias corrections were performed on the data depending on the availability of ground-truth points. Because of the relatively small elevation gradient, a single value is used to represent vertical bias across the landscape. We used this method as opposed to a traditional co-registration, which requires large enough snow-off surfaces at various points across the landscape to account for the lower point density of the snow-on data. In addition,

the 2016 flight contained the possibility for only two ground-truth points from the SNOTEL data (Deems et al., 2013).

The 2008 data was compared to 13 total points, combining field-based snow depth observations and SNOTEL data (Huntington, 2008). The median lidar height above ground was extracted with a search radius of three meters around each observation (Figure A2). The median of the combined points was taken to calculate a final vertical bias across the watershed. This general process was repeated for the other flights with minor modifications. For the 2016 flights, the median pixel height above Highway 89 was taken to represent a consistent snow-off surface. A DEM was created from the 2020 flight, and the 2014 DEM was used as the "truth". There were more than 50 snow-depth field observations for the 2022 flight, and the vertical bias was calculated similarly to the 2008 flight. The vertical biases between the flight and the ground-truth points were 0.03, 0.29, 0.35 0.44, 0.08, and 0.048 meters for the 2008, 2016 (03/26, 04/17, 05/18), 2020, and 2022 flights respectively.

Once the vertical bias was corrected, we classified the snow-off vegetation using a refined classification logic (Table A1; Figure 3; Figure 4) to produce four canopy strata classes: open, short, understory, and tall. In addition, an open-reference class represents open areas with a 1 m buffer around the canopy to mitigate edge effects for our analyses Figure A3). Snow depth was calculated by taking the height above ground rasters and filtering based on the canopy strata classifications (Table A2; Figure 5). Snow density was determined using the SnowPALM model, which models compaction as a function of albedo and density decay using values calibrated from SNOTEL sites (Broxton et al., 2015; see Equation 15). Where data was available, SnowPALM was validated against field and SNOTEL data (Huntington, 2008). In 2008, SnowPALM typically overpredicted density and

underpredicted snow depth. The median difference between SnowPALM and ground-truth density data was 0.02. We did not correct for this in our final SWE calculations. The model was run for each water year up until the flight dates. From depth and density, we calculated SWE, which was stored in both 1x1 m pixels and 30x30m grids.

We chose several key terrain variables to characterize the landscape as proxies for the energy and mass-balance dynamics that control snowpack accumulation and ablation. Northness (cos(aspect) * sin(slope)) primarily represents solar radiation while eastness (sin(aspect) * sin(slope)) represents wind loading that alters mass redistribution. Elevation correlates with both precipitation and temperature (Figure 1).

Forest structure metrics were chosen to be representative of the wide range of classifications that are used in other studies (e.g., Krogh et al., 2020; Mazzotti et al., 2020; Russell et al., 2021; Safa et al., 2021; Saksa et al., 2017). See Table A3 for forest structure classification descriptions. Most of the forest structure metrics were highly correlated (Figure A1). The fraction of vegetation (fVEG), a modified leaf area index (LAI'), and openness index are the metrics chosen to focus on for the remainder of the analyses after preliminary experiments with the RF model. fVEG is a broad forest structure metric that indicates the portion of a grid cell covered by pixels with maximum canopy height greater than three meters, impacting both the incoming radiation dynamics and interception (e.g., Mazzotti et al., 2019). LAI' is an index, calculated using a combination of a point density ratio and canopy height model (scaled to the maximum tree height), as a proxy for the total surface area of the leaves or needles on the canopy, acting as a limiting factor for canopy interception. This metric is then scaled to the maximum forest height (Krogh et al., 2020). Openness represents gap dynamics influencing incoming solar radiation and breaks in

potential interception. This metric is a ratio of the gap diameter (or twice the distance to nearest canopy) to the average forest height in a pixel. We took the natural log of this variable so that negative values represent forest gap to average tree height ratios less than one and positive values represent forest gap to average tree height ratios greater than one (Ellis et al., 2013).

Following the methodology of Varhola et al. (2010), SWE was normalized based on a "reference" value using Equation 1 below. This was done to control for precipitation and terrain differences across the study domain.

$$\Delta y = \frac{(x-R)}{R} * 100 \quad (1)$$

Δy represents the percent difference between the target pixel value (x) and a reference value (R). These percent change values were calculated for several inputs for our analyses. The general form of Equation 1 was applied to both pre- and post-disturbance analyses. Pre-disturbance, the goal was to determine how accumulation changed with increasing canopy cover. Open-reference areas were used as the reference sites. Post-disturbance, disturbed pixels were compared to undisturbed reference pixels (with higher fVEG).

2.2.1 Space for Structure Analysis

The space-for-structure approach aims to control for terrain and isolate secondary vegetation impacts on snow. The primary assumption associated with this method is that the dynamics dictated by the forest structure at one location are representative of dynamics that would occur if the structure at another location shifted towards the former. The space-for-structure analysis was run on the pre-disturbance accumulation and ablation metrics.

For the accumulation flights, the average SWE of all 1 m pixels within a 30m grid cell was taken to represent the target pixel SWE (x), and the average SWE of the open-reference 1 m pixels within a 30m grid cell was taken to represent the reference pixel SWE (R). The details of the open-reference approach are explained in Appendix A and Figure A3 and match the Varhola et al. framework. Low elevation areas (<2,100 m) were excluded from the 2016 and 2022 analyses due to ablation. The final metric is referred to as delta accumulation.

To calculate ablation, we took the SWE loss between each ablation season raster to produce an early season (March-April) and late season (April-May) ablation metric at the pixel level. We limited early season ablation to lower elevations (<2,100 m) and late season ablation to higher elevations (>2,100 m). Because of the limited temporal resolution of these data, if a pixel value was zero, we could not be sure when that pixel ablated completely. Thus, we excluded all zero-pixels in addition to any pixel that experienced accumulation.

For the ablation flights, we modified Equation 1 to create a normalized difference ablation metric (delta ablation).

$$\Delta y = \left[\frac{(x_i - x_f)}{x_i}\right]_t * 100 - \left[\frac{(x_i - x_f)}{x_i}\right]_o * 100 \quad (2)$$

Where x_i is initial SWE in the ablation period, x_f is final SWE in the ablation period, t is total area and o is open-reference area. Here, we calculated the percent of the total snowpack that ablated at the pixel level for all pixels and took the difference between the average total ablation in a 30m grid cell and the average open-reference ablation in a 30m grid cell. Thus, each side of the equation was calculated at the 1 m pixel scale and aggregated to the 30m scale before differencing.

2.2.2 Pre-Post Disturbance Analysis

The goal of the pre-post disturbance analysis was to develop a methodology to determine disturbance impacts on localized SWE accumulation. Thus, high elevations, which did not experience disturbance during the study period (>2200 m), were excluded from the pixels active in this analysis.

The search-algorithm analysis applied the space-for-structure approach to the post-disturbance flight (2022); however, instead of using an open-reference area as R, the goal was to identify undisturbed reference areas, typically with a *higher* fVEG than the thinned areas, to use as R. This method used a search function for each disturbed grid cell to identify undisturbed grid cells that were representative of the terrain, vegetation structure, and SWE of the disturbed grid cell prior to thinning. A Principal Component Analysis (PCA) was performed on the pre-disturbance data to determine reference areas using the prcomp package in R. Variables chosen to represent the target-reference pixel relationship were elevation, northness, eastness, fVEG, openness, and SWE from 03/26/2016. While an imperfect estimate, the 2016 SWE represents conditions closest to the 2022 SWE, allowing us to classify reference sites based on SWE relationships we would have expected without disturbance. The PCA resulted in four components, with the first three accounting for >80% of the variances. Using the scores from the individuals, we took the sum of squared distances (SSD) between the first three principal components between each disturbed grid cell and each undisturbed grid cell within a 660 m radius. Reference areas were identified using a minimum threshold SSD. For the pre-post disturbance analysis, the average 2022 SWE in the reference pixel was used as R and the average SWE in the target disturbed pixel is used as x (Equation 1).

We expanded our analysis to investigate pre-post disturbance SWE differences using a direct comparison approach with a simple normalized difference metric representing delta accumulation (Equation 3). Delta accumulation was calculated as

$$\Delta y = \left(\frac{x_d}{\overline{x_{td}}}\right) - \left(\frac{x_u}{\overline{x_{tu}}}\right) \quad (3)$$

where x represents the average SWE in a pixel, d represents disturbed grid cells (2022 data), t represents the entire domain, and u represents undisturbed grid cells (2016 data). This approach allowed us to compare grid cell-grid cell SWE data. Positive values indicate the disturbed grid cell contains more snow than the same grid cell pre-disturbance.

2.3 Random Forest (RF) Analysis

A RF model was created using the Ranger package in R (Wright & Ziegler, 2017) to determine controls on snowpack accumulation and ablation. RF classifiers utilize a set of regression trees created using bagged samples from a training dataset. We chose to use a RF model because it is an ensemble classifier that can be used with multi-modal data and accounts for covariance in the input variables. 75% of the samples were included in the training, or "in-bag" dataset for this study. The major input parameters that we altered were the number of decision trees (Ntree) and the number of variables to test at each "branch" (Mtry). Based on initial model runs, the error stabilized at ~300 trees, so for the rest of our analyses, we set Ntree to 300. Mtry was set to 3 to increase model robustness and because computational power was not limited (Belgiu & Drăgu, 2016).

We firstly performed RF analyses with Δy determined from Equation 1 and Equation 2 as the response variables. Predictor variables for the space-for-structure approach remained the same: elevation, northness, eastness, fVEG, openness, and LAI'. Accumulation rasters were run through the RF model using delta accumulation as the response variable

(Δy). This process was repeated for the ablation rasters using delta ablation as the response variable. For the pre-post disturbance analysis, all forest structure predictor variables were recalculated for the post-disturbance flight and only disturbed pixels were evaluated. In addition, the difference between fVEG in the disturbed and undisturbed reference areas (fVEG Disturbed – Reference) and the difference between fVEG pre- and post-disturbance (delta fVEG 2020-2014) were added as predictor variables.

2.4 Decision Support Tool

Based on the results of the RF models, we identified a series of "response" thresholds based on slope changes in select predictor variable partial plots. These thresholds represent areas where thinning impacts snowpack response (specifically delta accumulation response) in either positive (more accumulation) or negative (less accumulation) ways. We incorporated the results into a simple decision support tool. The goal was to capture forest structure thresholds that could be used to target forest structures for thinning. Using the Sagehen Project as a natural experiment, we tested these thresholds against actual disturbed areas to evaluate the effectiveness of thinning on snowpack resilience.

3 Results

3.1 Spatial Patterns of Snow and Forest Structure

Forest structure metrics are highly correlated (Figure A1). LAI', fVEG, and canopy density increase with elevation and northness. Openness shows the opposite trend, steadily decreasing with elevation and northness (Figure 6, Figure 7). Following expected terrain relationships, absolute SWE is greater at higher elevations on more northern-facing slopes in all three accumulation flights. Lower elevations have steady decreases in SWE in denser canopy, but as elevation increases, these relationships become less distinct (Figure 9, Figure A4). The relationships between SWE and terrain are nonlinear, in agreement with previous findings (e.g., Kirchner et al., 2014; Tennant et al., 2015; Varhola et al., 2010), and areas with lower SWE tend to be more variable in terms of fVEG and northness, particularly at higher elevations (Figure 9). R-squared values for SWE-elevation regressions are 0.51, 0.68, and 0.43 and slopes are 0.05, 0.19, and 0.09 for the 2008, 2016, and 2022 flights, respectively. R-squared values for SWE-fVEG regressions are 0.12, 0.09, and 0.02 and slopes are -23, -58, and -12 for the 2008, 2016, and 2022 flights respectively. $p < 0.001$ for all models (Figure A7).

3.2 Space-for-Structure Approach

A space for structure approach allows us to isolate the effects of vegetation structure by analyzing differences within 30m grid cells that we assume experience homogeneous precipitation and terrain. We isolate both coarse (fVEG) and fine (LAI', and openness) forest structures using lidar datasets. This approach is applied across three accumulation flights (2008, 2016, and 2022) and two ablation differences (March to April and April to May, 2016).

3.2.1 Accumulation

Delta accumulation patterns are in general agreement with data used in Varhola et al. (2010). With an increase in fVEG, delta accumulation decreases (becomes more negative), indicating that open areas accumulate more snow relative to overall pixel accumulation (Figure 10, Figure A5). Linear regressions of delta accumulation and fVEG with the lidar plots show greater variability and shallower slopes (-0.23, -0.37, and -0.15 for the 2008, 2016, and 2022 accumulation flights respectively) than the data used in the meta-analysis (-0.37; Table 1; Figure 11).

The RF models had varying levels of skill. R-squared values were 0.72, 0.62, and 0.16 for the 2008, 2016, and 2022 flights (Table 2). Forest structure metrics explained the greatest amount of variance in the model (Figure 13). Partial plots reveal more detailed dynamics and predict delta accumulation values between -4% and -20% (e.g., Figure 14), importantly always predicting that open reference sites accumulate more snow than forested sites. Decreasing delta accumulation indicates that the discrepancy between open and total grid cell SWE is increasing. Full partial plots can be seen in Figure A8, Figure A9, and Figure A10. Here, we emphasize patterns consistent across select flights. For the 2008 and 2016 flights, fVEG has the greatest importance on the RF models (Figure 13). There are distinct ranges of influence where certain variables predict greater change in delta accumulation. fVEG values < 0.3 predict consistent ~-5% delta accumulation (Figure 14a). At fVEG values > 0.3, these patterns become more variable, and decrease steeply until fVEG ~0.6 where the slope in the partial plot becomes shallower but continues to predict decreasing delta accumulation ~-15%. Qualitative thresholds can be observed for both LAI' and openness as well (Figure 14b,c). Delta accumulation maintains a maximum ~-10% until

openness reaches -2.5. A sharp decrease in delta accumulation is predicted until a minimum threshold at ~-17% delta accumulation and an openness index of 0 (Figure 14b). LAI' shows a steep decreasing trend from an LAI' of 0, with delta accumulation ~-4% to an LAI' of 0.2 and a delta accumulation minimum ~-11%. Northness and eastness showed inconsistent results with low importance and no clear trends across the flights. However, the 2008 flight, which best captures accumulation at lower elevations, indicates that southern-facing slopes experience a greater difference between open and under-canopy accumulation.

Response zones were chosen to define predicted snowpack response to thinning based on the thresholds addressed above (Figure 20, Figure 21). Low response zones are expected to experience the least amount of change post-thinning; high response zones are expected to benefit the most. Areas with lower absolute values of delta accumulation areas (values that approach zero) are places where we would expect greater total accumulation. For example, absolute SWE decreases with fVEG (Figure A4), and because the most important predictor variables (as determined by the RF model) show negative values of delta accumulation, grid cells where there is a greater difference (delta accumulation is more negative) have both higher fVEG and lower total SWE. Thus, as delta accumulation approaches zero, there is both lower fVEG and higher total SWE. Using these concepts, we identified high (fVEG>0.6 and openness<-2.5), low (fVEG<0.3 and openness>0), and moderate (all remaining) snowpack response areas. Low response areas are primarily at higher elevations, often in the steeper terrain, whereas high response areas tend to be in lower elevations and closer to the valley bottom. The classifications show clear differences in average delta accumulation from the space-for-structure approach of ~0, -10, and -30% across low to moderate to high, respectively (Figure 21b). Low response areas accumulate

more absolute SWE (60cm – 40cm from the low-high response areas), indicating they would not benefit as much from thinning.

3.2.2 Ablation

Ablation patterns using our modified equation (Equation 2) are more straightforward to interpret than the Varhola et al. (2010) delta ablation metric, but they cannot be directly compared due to this difference. Both delta ablation metrics show weak increasing linear trends with fVEG with r-squared values of 0.12 and 0.35 for the March-April and April-May flights respectively (Figure 12). This indicates that an increase in fVEG leads to a greater total grid cell ablation relative to the open reference pixels.

Elevation explains most of the variance in the RF model for the early season ablation (March-April), followed by fVEG and LAI' (RF r-squared of 0.52; Figure 15). Delta ablation increases as elevation, fVEG, and LAI' increase. An increase in openness predicts a general decrease in delta ablation, indicating that sites with more openness show less discrepancy between ablation in the open and under the canopy. fVEG also controls late season ablation (April-May; Figure 16). fVEG and openness explain most of the variance for late season ablation. Again, high-response regions emerge between ~-3-1 for openness and ~0.25-0.9 for fVEG.

3.3 Pre-Post Disturbance Approach

Clear patterns are not present between the delta accumulation metric and delta fVEG (disturbed – reference) using the searching algorithm (Figure A14). Despite the fact the search algorithm was able to identify at least one reference grid cell for almost every disturbed grid cell in our study domain (Figure A13), it did not provide easily interpreted results (Figure A15). The RF model was not as skillful as the overall space-for-structure

analyses (r-squared of 0.2, Table 3) and elevation showed the greatest importance on the model (Figure 17). Partial plots for the highest-importance variables (elevation, delta fVEG disturbed – reference areas, and delta fVEG 2020-2014) are inconsistent (Figure A15). With an increase in elevation and northness, the difference approaches 0 from -20% and -50% delta accumulation respectively (Figure A15). The delta fVEG (disturbed – reference) partial plot predicts that the difference between disturbed and reference sites increases (becomes more negative) as the delta fVEG (disturbed – reference) increases, indicating that undisturbed reference sites with more vegetation compared to the disturbed sites accumulate more snow (Figure A16).

The direct comparison approach was run on the entire domain as well as the isolated disturbed areas, and in either case delta accumulation was predicted primarily by elevation. The remainder of these results refer to the isolated disturbed analysis. The direct comparison approach increased the skill of the RF model (r-squared 0.40, Table 3). Terrain remained the most important metric (elevation, Figure 19). On average the RF model predicted positive delta accumulation values over the range of input variables (Figure A16). While the RF model predicts the that the difference between the disturbed and undisturbed delta accumulation decreases with elevation (from 30% to 0%), qualitative observations across the domain indicate the opposite (Figure 18). Delta accumulation peaks at 28% at an fVEG of ~0.65. Delta fVEG (2020 – 2014) predicts a negative trend in delta accumulation (with increasing delta fVEG), reaching a maximum around -65% delta fVEG at a delta accumulation of 35%.

4 Discussion

Snowpack accumulation and ablation in forests is fundamental to predicting water supplies and forest health in the Sierra Nevada (Barnhart et al., 2016; Godsey et al., 2014; Hammond et al., 2019; Harpold, Molotch, et al., 2014; Li et al., 2017). Sagehen Creek Basin is an example a heavily forested watershed where the snowpack is highly influence by vegetation (e.g., Kostadinov et al., 2019; Safa et al., 2021) that is undergoing forest treatments to reduce fire risk. However, few tools exist to quantify snowpack's response to vegetation, especially in complex terrain, motivating the development of the space-for-structure approach applied here. Our new method allows us to develop simple predictive relationships between forest structure and snow dynamics, which lay the groundwork for expanded analyses and management applications.

4.1 Comparison to the Varhola et al. (2010) Framework

We observe that accumulation shows a decreasing relationship with fVEG using our space-for-structure approach, matching the approach of Varhola et al. (2010). Using 2008 and 2016 flights that best approximate maximum accumulation, we find linear slopes of -0.23 and -0.37 delta accumulation/fVEG (Figure A7, r-squared of 0.72 and 0.62, respectively). These slopes are similar, though generally less than that from Varhola et al. (2010) of -0.37. We see more clear relationships in February 2008 but a lower slope, potentially due to the lack of ablation as compared to March 2016 (Figure 11). There was a much lower slope in March 2022, when ablation was substantial at lower elevations. Tradeoffs between accumulation and ablation processes are discussed in Section 4.2. In general, the correspondence between 2008 and 2016 support the space-for-structure approach and the resulting process inferences. In addition to reproducing the SWE versus

forest cover linear relationships by Varhola et al. (2010), we also use a random forest (RF) model to demonstrate the importance of the fraction of vegetation in a grid cell (fVEG), which accounts for the most variation in two of the accumulation models. The RF results support the weaker effects of fVEG on SWE in 2008 versus 2016 (Figure 14) and hint at a much lower slope (less effects on snow) when forest cover is below ~30%. The much lower slopes in the RF partial plots (~0.1 % delta accumulation /% fVEG) and higher r-squared values as compared to the linear relationships, suggest that other factors may contribute besides fVEG.

We apply a similar open reference site (space-for-structure) approach to quantify the effects of disturbance using pre- and post-disturbance lidar flights but find more noisy results in 2022. A simple normalized difference approach (Figure 18) shows the importance of elevation on post-disturbance snowpack, consistent with the RF analysis (Figure 17). This elevation signal may be due to a combination of snowfall and ablation distribution causing more snow loss at lower elevations in 2022 as compared to 2016 (Figure 2). The lack of signal from delta fVEG (2020 – 2014) in the RF analysis makes it difficult to draw conclusions from these results. However, among only disturbed areas (Figure A16), there is a clearer signal supporting our hypothesis that predicts that as a disturbed site loses more vegetation, there will be more snow in the disturbed site relative to the same pixel in 2016 (Figure A16). In this case SWE is maximized at ~65% vegetation loss with 30% greater SWE in the disturbed site. The search algorithm analysis (Figure A15) did not support our hypothesis and predicted more snow in reference areas. Because we hypothesize (and observed through field validation) that snow disappears under the canopy before open spaces, both pre-post methods employed here could be weakened by areas with no snow

under canopy, which was widespread in 2022. Differences in snowfall distribution, confounding ablation effects of accumulation, and challenges quantifying changes in forest cover increase the appeal of a space-for-structure approach over the pre-post methods used in this study.

Our space-for-structure approach predicts greater ablation with increasing fVEG, opposite of the relationships found by Varhola et al. (2010) and Krogh et al. (2020) but consistent with process-based studies in warmer climates (Kostadinov et al., 2019; Lundquist et al., 2013; Safa et al., 2021). These studies find that in warmer climates, a combination of the timing of the ablation season (April-May, when solar irradiance is relatively low) and higher temperatures results in "warm" trees that emit enough longwave radiation to dominate energy fluxes that control ablation. We find average ablation slopes of 0.8 and 0.6 (% delta ablation/fVEG) for the March-April and April-May period (r-squared of 0.51 and 0.55, Figure 12). Partial plots in the RF model also show positive slopes with fVEG but indicate that there is little effect of canopy when fVEG is below ~30% (Figure 16). Ablation rates calculated between two lidar flights are fundamentally different than season-long ablation metrics used by Varhola et al. (2010). In particular, the lidar-based ablation metrics are subject to differences in precipitation amount, cold content, energy inputs, and other factors that are highly spatially variable. We attempted to mitigate some of these issues using early season (lower elevation) and late season (higher elevation) ablation windows and controlling for initial SWE in each case. However, issues remain in our approach that could be improved. For example, including snow disappearance date (with modeling or optical remote sensing, for example) would allow us to calculate rate of ablation spatially and help solve some of the temporal issues requiring normalization. Despite these issues, multi-

temporal lidar datasets offer the potential for ablation calculations that have previously not been possible.

4.2 Role of Finer-Scale Forest Structure and Terrain on Snow Dynamics

Our space-for-structure approach suggests that coarse and fine-scale forest structure are important predictors of snow accumulation, explaining more variation in accumulation patterns in dense forests than terrain features like elevation, slope, and aspect. The predictor importance from the RF model (e.g., Figure 13) show that fVEG, LAI', and openness are more important than terrain metrics (elevation, northness, and eastness) for predicting our delta accumulation metric, demonstrating the value of the open reference site approach. The partial plots from the RF model (Figure 14) consistently show a non-linear effect on accumulation from LAI' and openness, as compared to a more linear relation with fVEG. Overall, the results imply that vegetation has the largest role in reducing snow accumulation when fVEG is high (>0.6), openness is high (vegetation height<=canopy gap diameter), and LAI' is high (>0.25). Importantly, this indicates that a canopy gap to vegetation height ratio <1 optimizes accumulation, in general support of earlier studies that predicted gap influences are maximized when shading from nearby canopy is high and canopy gap to forest height ratios are <1 (Anderson, 1956; Musselman et al., 2015). Conversely, partial plots for terrain effects on accumulation and ablation are weaker with more mixed slopes across flights (Figure 14). From the 2008 partial plots, our results match Krogh et al. (2020) who modeled that lower-elevation, south-facing slopes experienced post-thinning increases in accumulation. Both 2016 and 2008 accumulation suggest lower elevations as potentially more responsive to thinning (discussed more in Section 4.3). The dominance of vegetation features in our prediction of snow accumulation compared to previous lidar analyses (e.g.,

Safa et al., 2021; Tennant et al., 2015) is because of the open reference approach and improved snow density modeling allowing us to calculate SWE (rather than snow depth).

Snow ablation analyses also point to the importance of fine-scale forest structure despite our space-for-structure approach not effectively accounting for different energy environments. Our method shows promise, but lacks important energy balance factors, like increased solar irradiance later in the melt season or differences in snowpack cold content, that make interpreting our results more challenging. Because of differences in energy environments, elevation ranks high in terms of importance (Figure 15), but fVEG, openness, and LAI' are more important during the early ablation estimate. Both early and late season ablation estimates indicate a balance between fVEG (lowest ablation <~50%) and openness (lowest ablation ≥~1:1 gap width: tree height) to promote retention (Figure 16). The importance of openness in the accumulation and ablation analysis suggests that forest thinning that reduces fVEG and openness will increase accumulation and but forest thinning that increases openness will decrease ablation, potentially increasing snow retention in open areas.

Our results begin to unravel the role of coarse and fine-scale forest structure metrics on snow accumulation and ablation in ways that match process understanding being made with fine-scale forest modeling and field observations. In particular, we show that despite the importance of a coarse (simpler) fVEG metric based only on tree spatial coverage, we find that metrics that account for vertical point density (LAI') and horizontal and vertical information (openness) can provide substantial additional information. It's worth noting that these metrics are highly correlated across the full domain (Figure A1), but their correlation within individual elevation bands (Figure 6) is more mixed due to differences in forest

species, terrain, land use history, and other unaccounted factors. fVEG is the most important vegetation factor compared to openness and LAI', varies more linearly, is easier to estimate, and matches the Varhola et al. (2010) framework. Importantly, however, Varhola et al. (2010) emphasized the inconsistencies between forest structure metrics across studies. We experimented with several forest structure metrics based on height and point density to account for these inconsistencies, and narrowed our metrics based on preliminary RF runs and knowledge about specific density metrics that have been found to be important in this region (Krogh et al., 2020; Safa et al., 2021). The potential versatility in chosen metrics would allow different configuration of our RF modeling approach in future studies.

4.3 Management applications and future research directions

Our results indicate that while simple linear models capture broad patterns of forest-snow interactions, thresholds at which specific forest structure metrics become more or less important can help refine the management of forests similar to SCB. We developed a decision support tool for SCB (Figure 21) using clear thresholds in fVEG and openness (Figure 20, Figure 14) to define high, moderate, and low response of SWE to thinning. These variables represent the interplay between coarse and fine-scale forest structure in ways that are more distinct than LAI' (Figure 14). We find less negative delta accumulation and more absolute SWE in the low response areas (Figure 20) suggesting that our threshold method has successfully identified areas where snow accumulation would not be likely to increase if the forest was thinned. These areas account for a small portion (~7%) of the total domain, suggesting that forest thinning has the potential to increase snow in widespread areas of SCB. The Sagehen Project was developed with extensive ecosystem considerations, focused on wildlife and fire, leading to a variety of thinning and restoration

techniques being applied to the SCB (Figure 1). Overall, 29% of the treated areas as part of the Sagehen Project were high response areas and 27% were moderate response. While the resilience of snowmelt-derived water resources was not an explicit priority for the Sagehen Project, we observe potential co-benefits to managing towards ecosystem resilience of wildlife and fire for snow accumulation and retention in this area of the central Sierra Nevada. Our decision support tool for SCB could be expanded to other areas with similar snow-on and snow-off datasets. The decision support tool offers both a retrospective means to assess restoration effectiveness (as done in this study) as well as a tool for proactive planning efforts.

Several key efforts could help advance our method and increase its impact in future management and research applications. A more robust method for determining vegetation thresholds might divide the domain by forest and vegetation ecotones. For example, the 1.5 meter threshold for short vegetation and understory classifications could be refined using vegetation maps to determine shrub and grass height as well as understory height. Incorporating canopy type into these analyses would also improve management implications. Future work may wish to take a similar approach with refined forest structure metrics in the RF model, such as those that incorporate edginess metrics derived with aspect (Broxton et al., 2021; Currier et al., 2019; Mazzotti et al., 2019, 2020). In addition, these results could be impacted by pixel bias because there are typically more returns (and, thus pixels) in open areas (See Appendix A for more details). Our processing method attempts to mitigate data losses due to conflation with canopy, but there are opportunities for improvement within the workflow. The analyses could be improved with increased point density in the snow-on flights that better resolve near and under canopy snowpack. While the point density was high

in 2022, the pre- and post-disturbance analysis was complicated by the timing of the snow-on flight. With a future of less certain snowpack accumulation trends, data collection may have to account for earlier peak SWE to ensure ablation signals are mitigated.

Overall, the space-for-structure approach we developed here accounts for local variation in precipitation and energy budgets in ways that allows new insights into snow-vegetation interactions and has potential for transferability to other sites. We observe consistency across years with varying antecedent conditions (pre-disturbance), with larger differences in delta accumulation in 2016 reflecting potential ablation signals that accentuate larger SWE values in open areas. Because this framework allows for the isolation of fine-scale forest structure metrics and can be used on multi-temporal data, it presents a unique opportunity to understand broad-scale dynamics across climate regimes using consistent methodology, similar to Safa et al., 2021. Ablation signals are a potential new source of information, but also present challenges to developing methods to correct for differences in energy budgets with temporally distributed data that could capture changes in solar irradiance, for example. We expect expansion and improvement on this method that take advantage of the open-source, consistent data processing approaches (including those presented in this study) and newly available lidar datasets.

5 Conclusion

Scientists have been working to constrain the impacts of forests on snow for over 50 years and there are efforts that go all the way from continuous modeling at fine scales to disturbance analyses at watershed scales. This project contributes to a growing body of work that seeks to understand how forest and snowpack interact in disturbance-impacted landscapes. We present new methods for processing high-resolution, spatially-distributed lidar data that have the ability to enhance classifications of fine-scale forest structure metrics in relation to snowpack.

An increase in remote sensing data has caused a revolution with lidar, which has the ability shift our scientific paradigm, but we have to be able to get the data into a consistent format and analyze it in consistent ways. It is also critical that we integrate natural and climate-caused variability into our studies, utilizing an integrated approach to studying complex systems. Our space-for-structure analyses support previous findings about open versus under-canopy snowpack and more specific coarse-scale forest structure metrics (fVEG) while expanding to identify thresholds in critical fine-scale forest structure metrics (openness) that can be utilized to determine whether management practices integrate hydrological benefits. The decision support tool created here has potential to allow managers to use these critical structure thresholds to determine how comprehensive resilience classifications are. For example, decreasing fVEG from 0.6 to 0.3 has drastic impacts on how much snow accumulated in the open space in a grid cell relative to the rest of the cell.

Ablation dynamics and pre-post disturbance analyses have presented even more challenges, driven by temporal limitations of lidar. Rapid disturbance and restoration

projects are actively altering our forests, and an increase in multi-temporal lidar datasets could drastically improve our ability to better constrain these metrics.

This project contributes to a growing body of work that seeks to understand how forest and snowpack interact in disturbance impacted landscapes. We present new methods for processing high-resolution, spatially-distributed lidar data that have the ability to enhance classifications of fine-scale forest structure metrics in relation to snowpack.

References

Anderson, H. W. (1956). Forest-cover effects on snowpack accumulation and melt, Central Sierra Snow Laboratory. *Transactions, American Geophysical Union*, *37*(3), 307. https://doi.org/10.1029/TR037i003p00307

Bales, R. C., Molotch, N. P., Painter, T. H., Dettinger, M. D., Rice, R., & Dozier, J. (2006). Mountain hydrology of the western United States. *Water Resour. Res*, *42*, 8432. https://doi.org/10.1029/2005WR004387

Barnett, T. P., Adam, J. C., & Lettenmaier, D. P. (2005). Potential impacts of a warming climate on water availability in snow-dominated regions. *Nature 2005 438:7066*, *438*(7066), 303–309. https://doi.org/10.1038/nature04141

Barnhart, T. B., Molotch, N. P., Livneh, B., Harpold, A. A., Knowles, J. F., & Schneider, D. (2016). Snowmelt rate dictates streamflow. *Geophysical Research Letters*, *43*(15), 8006–8016. https://doi.org/10.1002/2016GL069690

Bart, R. R., Ray, R. L., Conklin, M. H., Safeeq, M., Saksa, P. C., Tague, C. L., & Bales, R. C. (2021). Assessing the effects of forest biomass reductions on forest health and streamflow. *Hydrological Processes*. https://doi.org/10.1002/hyp.14114

Belgiu, M., & Drăgu, L. (2016). Random forest in remote sensing: A review of applications and future directions. *ISPRS Journal of Photogrammetry and Remote Sensing*, *114*, 24–31. https://doi.org/10.1016/J.ISPRSJPRS.2016.01.011

Boisramé, G. F. S., Thompson, S. E., Tague, C. (Naomi), & Stephens, S. L. (2019). Restoring a Natural Fire Regime Alters the Water Balance of a Sierra Nevada Catchment. *Water Resources Research*. https://doi.org/10.1029/2018WR024098

Broxton, P. D., Harpold, A. A., Biederman, J. A., Troch, P. A., Molotch, N. P., & Brooks, P. D. (2015). Quantifying the effects of vegetation structure on snow accumulation and ablation in mixed-conifer forests. *Ecohydrology*, *8*(6), 1073–1094. https://doi.org/10.1002/eco.1565

Broxton, P. D., Moeser, C. D., & Harpold, A. (2021). Accounting for Fine-Scale Forest Structure is Necessary to Model Snowpack Mass and Energy Budgets in Montane Forests. *Water Resources Research*, *57*(12), e2021WR029716. https://doi.org/10.1029/2021WR029716

Butler, H., Chambers, B., Hartzell, P., & Glennie, C. (2020). PDAL: An open source library for the processing and analysis of point clouds. *Computers & Geosciences*, 104680. https://doi.org/10.1016/j.cageo.2020.104680

Cooper, A. E., Kirchner, J. W., Wolf, S., Lombardozzi, D. L., Sullivan, B. W., Tyler, S. W., & Harpold, A. A. (2020). Snowmelt causes different limitations on transpiration in a Sierra Nevada conifer forest. *Agricultural and Forest Meteorology*, *291*, 108089. https://doi.org/10.1016/j.agrformet.2020.108089

Currier, W. R., & Lundquist, J. D. (2018). Snow Depth Variability at the Forest Edge in Multiple Climates in the Western United States. *Water Resources Research*, *54*(11), 8756–8773. https://doi.org/10.1029/2018WR022553

Currier, W. R., Pflug, J., Mazzotti, G., Jonas, T., Deems, J. S., Bormann, K. J., Painter, T. H., Hiemstra, C. A., Gelvin, A., Uhlmann, Z., Spaete, L., Glenn, N. F., & Lundquist, J. D. (2019). Comparing Aerial Lidar Observations With Terrestrial Lidar and Snow-Probe Transects From NASA's 2017 SnowEx Campaign. *Water Resources Research*, *55*(7), 6285–6294. https://doi.org/10.1029/2018WR024533

Dalponte, M., & Coomes, D. A. (2016). Tree-centric mapping of forest carbon density from airborne laser scanning and hyperspectral data. *Methods in Ecology and Evolution*, *7*(10), 1236–1245. https://doi.org/10.1111/2041-210X.12575

Deems, J. S., Painter, T. H., & Finnegan, D. C. (2013). Lidar measurement of snow depth: a review. *Journal of Glaciology*, *59*(215). https://doi.org/10.3189/2013JoG12J154

Dickerson-Lange, S. E., Vano, J. A., Gersonde, R., & Lundquist, J. D. (2021). Ranking Forest Effects on Snow Storage: A Decision Tool for Forest Management. *Water Resources Research*, *57*. https://doi.org/10.1029/2020WR027926

Dozier, J. ;, & Painter, T. H. (2004). MULTISPECTRAL AND HYPERSPECTRAL REMOTE SENSING OF ALPINE SNOW PROPERTIES. In *Annual Review of Earth and Planetary Sciences* (Vol. 32).

Du, E., Link, T. E., Wei, L., & Marshall, J. D. (2016). Evaluating hydrologic effects of spatial and temporal patterns of forest canopy change using numerical modelling. *Hydrological Processes*, *30*(2), 217–231. https://doi.org/10.1002/HYP.10591

Ellis, C. R., Pomeroy, J. W., & Link, T. E. (2013). Modeling increases in snowmelt yield and desynchronization resulting from forest gap-thinning treatments in a northern mountain headwater basin. *Water Resources Research*, *49*(2), 936–949. https://doi.org/10.1002/WRCR.20089

Gatziolis, D., & Andersen, H.-E. (2008). *A Guide to LIDAR Data Acquisition and Processing for the Forests of the Pacific Northwest*.

GDAL/OGR contributors. (2020). *GDAL/OGR Geospatial Data Abstraction software Library*. Retrieved from https://gdal.org.

Godsey, S. E., Kirchner, J. W., & Tague, C. L. (2014). Effects of changes in winter snowpacks on summer low flows: case studies in the Sierra Nevada, California, USA. *Hydrological Processes*, *28*(19), 5048–5064. https://doi.org/10.1002/hyp.9943

Graup, L. (2021). *Preserving Mountains with Forest Management, CA 2020*.

Guo, Q. (2014). *Full Waveform LiDAR Survey of Tahoe National Forest*.

Hammond, J. C., Harpold, A. A., Weiss, S., & Kampf, S. K. (2019). Partitioning snowmelt and rainfall in the critical zone: effects of climate type and soil properties. *Hydrology and Earth System Sciences*, *23*(9), 3553–3570. https://doi.org/10.5194/hess-23-3553-2019

Harder, P., Pomeroy, J. W., Helgason, W. D., & Helgason, W. D. (2020). Improving sub-canopy snow depth mapping with unmanned aerial vehicles: Lidar versus structure-from-motion techniques. *Cryosphere*, *14*(6), 1919–1935. https://doi.org/10.5194/tc-14-1919-2020

Harpold, A. A., Dettinger, M., & Rajagopal, S. (2017). Defining Snow Drought and Why It Matters. *EOS*. http://drought.unl.edu/DroughtBasics/TypesofDrought.aspx

Harpold, A. A., Guo, Q., Molotch, N., Brooks, P. D., Bales, R., Fernandez-Diaz, J. C., Musselman, K. N., Swetnam, T. L., Kirchner, P., Meadows, M. W., Flanagan, J., & Lucas, R. (2014). LiDAR-derived snowpack data sets from mixed conifer forests across the Western United States. *Water Resources Research*, *50*(3), 2749–2755. https://doi.org/10.1002/2013WR013935

Harpold, A. A., Krogh, S. A., Kohler, M., Eckberg, D., Greenberg, J., Sterle, G., & Broxton, P. D. (2020). Increasing the efficacy of forest thinning for snow using high-resolution modeling: A proof of concept in the Lake Tahoe Basin, California, USA. *Ecohydrology*, *13*(4), e2203. https://doi.org/10.1002/ECO.2203

Harpold, A. A., Molotch, N. P., Musselman, K. N., Bales, R. C., Kirchner, P. B., Litvak, M., & Brooks, P. D. (2014). Soil moisture response to snowmelt timing in mixed-conifer subalpine forests. *Hydrological Processes*, *29*(12), 2782–2798. https://doi.org/10.1002/hyp.10400

Hopkins, C., Sitar, M., Chasmer, L., & Treitz, P. (2004). Mapping Snowpack Depth beneath Forest Canopies Using Airborne Lidar. *Photogrammetric Enginering & Remote Sensing*, *70*(3), 323–330.

Hopkinson, C., Pomeroy, J., Debeer, C., Ellis, C., & Anderson, A. (2010). *Relationships between snowpack depth and primary LiDAR point cloud derivatives in a mountainous environment. 352*.

Hubbart, J. A., Link, T. E., & Gravelle, J. A. (2015). Forest Canopy Reduction and Snowpack Dynamics in a Northern Idaho Watershed of the Continental-Maritime Region, United States. *Forest Science*, *61*(5), 882–894. https://doi.org/10.5849/FORSCI.14-025

Huning, L. S., & AghaKouchak, A. (2018). Mountain snowpack response to different levels of warming. *Proceedings of the National Academy of Sciences of the United States of America*, *115*(43), 10932–10937. https://doi.org/10.1073/PNAS.1805953115/-/DCSUPPLEMENTAL

Huntington, J. (2008). *Snowpack measurement in the Sierra Nevada.*

Jost, G., Weiler, M., Gluns, D. R., & Alila, Y. (2007). The influence of forest and topography on snow accumulation and melt at the watershed-scale. *Journal of Hydrology*, *347*(1–2), 101–115. https://doi.org/10.1016/J.JHYDROL.2007.09.006

Kirchner, J., Brown, J., & Horne, A. (2005). *Vision for the University of California, Berkeley, Sagehen Creek Field Station.*

Kirchner, P. B., Bales, R. C., Molotch, N. P., Flanagan, J., & Guo, Q. (2014). LiDAR measurement of seasonal snow accumulation along an elevation gradient in the southern Sierra Nevada, California. *Hydrology and Earth System Sciences*. https://doi.org/10.5194/hess-18-4261-2014

Kostadinov, T. S., Schumer, R., Hausner, M., Bormann, K. J., Gaffney, R., McGwire, K., Painter, T. H., Tyler, S., & Harpold, A. A. (2019). Watershed-scale mapping of fractional snow cover under conifer forest canopy using lidar. *Remote Sensing of Environment*, *222*, 34–49. https://doi.org/10.1016/j.rse.2018.11.037

Krogh, S. A., Broxton, P. D., Manley, P. N., & Harpold, A. A. (2020). Using Process Based Snow Modeling and Lidar to Predict the Effects of Forest Thinning on the Northern Sierra Nevada Snowpack. *Frontiers in Forests and Global Change*, *3*, 21. https://doi.org/10.3389/ffgc.2020.00021

Li, D., Wrzesien, M. L., Durand, M., Adam, J., & Lettenmaier, D. P. (2017). How much runoff originates as snow in the western United States, and how will that change in the future? *Geophysical Research Letters*, *44*(12), 6163–6172. https://doi.org/10.1002/2017GL073551

Lindstom, S., Rucks, P., & Wigand, P. (1999). A contextual overview of human land use and environmental conditions. In *Lake Tahoe Watershed Assessment* (Vol. 1). Pacific Southwest Research Station, Forest Service, US Department of Agriculture.

Lundquist, J. D., Dickerson-Lange, S. E., Lutz, J. A., & Cristea, N. C. (2013). Lower forest density enhances snow retention in regions with warmer winters: A global framework developed from plot-scale observations and modeling. *Water Resources Research*, *49*(10), 6356–6370. https://doi.org/10.1002/wrcr.20504

Lundquist, J. D., & Loheide, S. P. (2011). How evaporative water losses vary between wet and dry water years as a function of elevation in the Sierra Nevada, California, and critical factors for modeling. *Water Resources Research*, *47*(3). https://doi.org/10.1029/2010WR010050

Mast, M. A., & Clow, D. W. (2000). *Environmental characteristics and water-quality of Hydrologic Benchmark Network stations in the Western United States*.

Mazzotti, G., Currier, W. R., Deems, J. S., Pflug, J. M., Lundquist, J. D., & Jonas, T. (2019). Revisiting Snow Cover Variability and Canopy Structure Within Forest Stands: Insights From Airborne Lidar Data. *Water Resources Research*, *55*(7), 6198–6216. https://doi.org/10.1029/2019WR024898

Mazzotti, G., Essery, R., Moeser, C. D., & Jonas, T. (2020). Resolving Small-Scale Forest Snow Patterns Using an Energy Balance Snow Model With a One-Layer Canopy. *Water Resources Research*, *56*(1). https://doi.org/10.1029/2019WR026129

Moeser, C. D., Broxton, P. D., Harpold, A., & Robertson, A. (2020). Estimating the Effects of Forest Structure Changes From Wildfire on Snow Water Resources Under Varying Meteorological Conditions. *Water Resources Research*, *56*(11), e2020WR027071. https://doi.org/10.1029/2020WR027071

Moser, S., Franco, G., Pittiglio, S., Chou, W., & Cayan, D. (2009). *The Future is Now: An Update on Climate Change Science Impacts and Response Options for California*.

Musselman, K. N., Molotch, N. P., Margulis, S. A., Kirchner, P. B., & Bales, R. C. (2012). Influence of canopy structure and direct beam solar irradiance on snowmelt rates in a mixed conifer forest. *Agricultural and Forest Meteorology*, *161*, 46–56. https://doi.org/10.1016/j.agrformet.2012.03.011

Musselman, K. N., Pomeroy, J. W., & Link, T. E. (2015). Variability in shortwave irradiance caused by forest gaps: Measurements, modelling, and implications for snow energetics. *Agricultural and Forest Meteorology*, *207*, 69–82. https://doi.org/10.1016/j.agrformet.2015.03.014

North, M. (2012). *Managing Sierra Nevada Forests*.

Painter, T. H., Berisford, D. F., Boardman, J. W., Bormann, K. J., Deems, J. S., Gehrke, F., Hedrick, A., Joyce, M., Laidlaw, R., Marks, D., Mattmann, C., McGurk, B., Ramirez, P., Richardson, M., Skiles, S. M. K., Seidel, F. C., & Winstral, A. (2016). The Airborne Snow Observatory: Fusion of scanning lidar, imaging spectrometer, and physically-based modeling for mapping snow water equivalent and snow albedo. *Remote Sensing of Environment*, *184*, 139–152. https://doi.org/10.1016/J.RSE.2016.06.018

Piske, C. (2022). *Using Lidar to Investigate Forest-Snow Interactions in a High Elevation Critical Zone*.

Rakhmatulina, E., Boisramé, G., Stephens, S. L., & Thompson, S. (2021). Hydrological Benefits of Restoring Wildfire Regimes in the Sierra Nevada Persist in a Warming Climate. *Journal of Hydrology*, *593*. https://doi.org/10.1016/j.jhydrol.2020.125808

Roussel, J., & Auty, D. (n.d.). Airborne LiDAR Data Manipulation and Visualization for Forestry Applications. In *R package version 4.0.1*. https://cran.r-project.org/package=lidR.

Roussel, J.-R., Auty, D., Coops, N. C., Tompalski, P., Goodbody, T. R. H., Meador, A. S., Bourdon, J.-F., de Boissieu, F., & Achim, A. (2020). lidR: An R package for analysis of Airborne Laser Scanning (ALS) data. *Remote Sensing of Environment*, *251*, 112061. https://doi.org/10.1016/j.rse.2020.112061

Russell, M., Eitel, J. U. H., Link, T. E., & Silva, C. A. (2021). Important Airborne Lidar Metrics of Canopy Structure for Estimating Snow Interception. *Remote Sensing 2021, Vol. 13, Page 4188*, *13*(20), 4188. https://doi.org/10.3390/RS13204188

Safa, H., Krogh, S. A., Greenberg, J., Kostadinov, T. S., & Harpold, A. A. (2021). Unraveling the Controls on Snow Disappearance in Montane Conifer Forests Using Multi-Site Lidar. *Water Resources Research*, *57*(12). https://doi.org/10.1029/2020WR027522

Sagehen Project. (2013).

Saksa, P. C., Conklin, M. H., Battles, J. J., Tague, C. L., & Bales, R. C. (2017). Forest thinning impacts on the water balance of Sierra Nevada mixed-conifer headwater basins. *Water Resources Research*, *53*(7), 5364–5381. https://doi.org/10.1002/2016WR019240

Schneider, E. E., Affleck, D. L. R., & Larson, A. J. (2019). *Tree spatial patterns modulate peak snow accumulation and snow disappearance*. https://doi.org/10.1016/j.foreco.2019.03.031

Serreze, M. C., Clark, M. P., Armstrong, R. L., McGinnis, D. A., & Pulwarty, R. S. (1999). Characteristics of the western United States snowpack from snowpack telemetry (SNOTEL) data. *Water Resources Research*, *35*(7), 2145–2160. https://doi.org/10.1029/1999WR900090

Stephens, S. L., Thompson, S., Boisramé, G., Collins, B. M., Ponisio, L. C., Rakhmatulina, E., Steel, Z. L., Stevens, J. T., van Wagtendonk, J. W., & Wilkin, K. (2021). Fire, water, and biodiversity in the Sierra Nevada: a possible triple win. *Environmental Research Communications*, *3*(8), 081004. https://doi.org/10.1088/2515-7620/AC17E2

Stevens, J. T. (2017). Scale-dependent effects of post-fire canopy cover on snowpack depth in montane coniferous forests. *Ecological Applications*, *27*(6), 1888–1900. https://doi.org/10.1002/EAP.1575

Tennant, C. J., Crosby, B. T., & Godsey, S. E. (2015). Elevation-dependent responses of streamflow to climate warming. *Hydrological Processes*, *29*(6), 991–1001. https://doi.org/10.1002/hyp.10203

Tennant, C. J., Harpold, A. A., Lohse, K. A., Godsey, S. E., Crosby, B. T., Larsen, L. G., Brooks, P. D., van Kirk, R. W., & Glenn, N. F. (2017). Regional sensitivities of seasonal snowpack to elevation, aspect, and vegetation cover in western North America. *Water Resources Research*. https://doi.org/10.1002/2016WR019374

Tinkham, W. T., Smith, A. M. S., Marshall, H. P., Link, T. E., Falkowski, M. J., & Winstral, A. H. (2014). Quantifying spatial distribution of snow depth errors from LiDAR using Random Forest. *Remote Sensing of Environment*, *141*, 105–115. https://doi.org/10.1016/J.RSE.2013.10.021

Trujillo, E., & Molotch, N. P. (2014). Snowpack regimes of the Western United States. *Water Resources Research*, *50*(7), 5611–5623. https://doi.org/10.1002/2013WR014753

Vaillant, N. M., & Stephens, S. L. (2009). Fire history of a lower elevation Jeffrey pine-mixed conifer forest in the eastern Sierra Nevada, California, USA. *Fire Ecology*, *5*(3), 4–19. https://doi.org/10.4996/fireecology.0503004

Varhola, A., Coops, N. C., Weiler, M., & Moore, R. D. (2010). Forest canopy effects on snow accumulation and ablation: An integrative review of empirical results. In *Journal of Hydrology* (Vol. 392, Issues 3–4, pp. 219–233). Elsevier. https://doi.org/10.1016/j.jhydrol.2010.08.009

Washoe Tribe. (2021). *Wa She Shu: The Washoe People Past and Present*.

Webster, C., Mazzotti, G., Essery, R., & Jonas, T. (2020). Enhancing airborne LiDAR data for improved forest structure representation in shortwave transmission models. *Remote Sensing of Environment*, *249*, 112017. https://doi.org/10.1016/j.rse.2020.112017

Wright, M. N., & Ziegler, A. (2017). ranger: A fast implementation of random forests for high dimensional data in C++ and R. *J Stat Softw*, *77*, 1–17.

Xu, Q., Man, A., Fredrickson, M., Hou, Z., Pitkänen, J., Wing, B., Ramirez, C., Li, B., & Greenberg, J. A. (2018). Quantification of uncertainty in aboveground biomass estimates derived from small-footprint airborne LiDAR. *Remote Sensing of Environment*, *216*, 514–528. https://doi.org/10.1016/J.RSE.2018.07.022

Zheng, Z., Ma, Q., Jin, S., Su, Y., Guo, Q., & Bales, R. C. (2019). Canopy and Terrain Interactions Affecting Snowpack Spatial Patterns in the Sierra Nevada of California. *Water Resources Research*, *55*(11), 8721–8739. https://doi.org/10.1029/2018WR023758

Tables

Table 1: Linear Regressions, Delta Snowpack Accumulation/Ablation vs. Fraction of Vegetation

Date	P-Value	R-Squared	Residual Std. Error	Slope
02/10/2008	<0.001	0.63	4.1	-0.23
03/26/2016*	<0.001	0.31	11.6	-0.34
03/26/2016	<0.001	0.23	15.4	-0.37
03/21/2022*	<0.001	0.058	12.8	-0.15
03/21/2022	<0.001	0.016	13.5	-0.084
March-April	0.01	0.13	10.4	0.17
April-May	<0.001	0.34	3.52	0.13

Note: *Elevations limited to >2100m

Table 2. Random Forest Model Results, Space for Structure Analysis

Date	OOB R-Squared	OOB MSE
02/10/2008	0.72	12.21
03/26/2016*	0.62	73.28
03/21/2022*	0.16	157.44
March-April	0.51	63.88
April-May	0.72	73.28

Note: *Elevations limited to >2100m
OOB – out of bag, MSE – mean squared error.
Response variables are delta accumulation and delta ablation. Predictor variables include elevation. fVEG, LAI', openness, eastness, and northness.

Table 3. Random Forest Model Post Disturbance Analysis

Date	OOB R-Squared	OOB MSE
Ref. Search	0.20	919
Dir. Compare (all)	0.71	0.02
Dir. Compare (disturbed)	0.42	0.02

Note: *Elevations limited to >2100m
OOB – out of bag, MSE – mean squared error.
Response variable is delta accumulation. Predictor variables include elevation. fVEG, LAI', delta fVEG (2020-2014), delta fVEG (disturbed-reference)openness, eastness, and northness

Figures

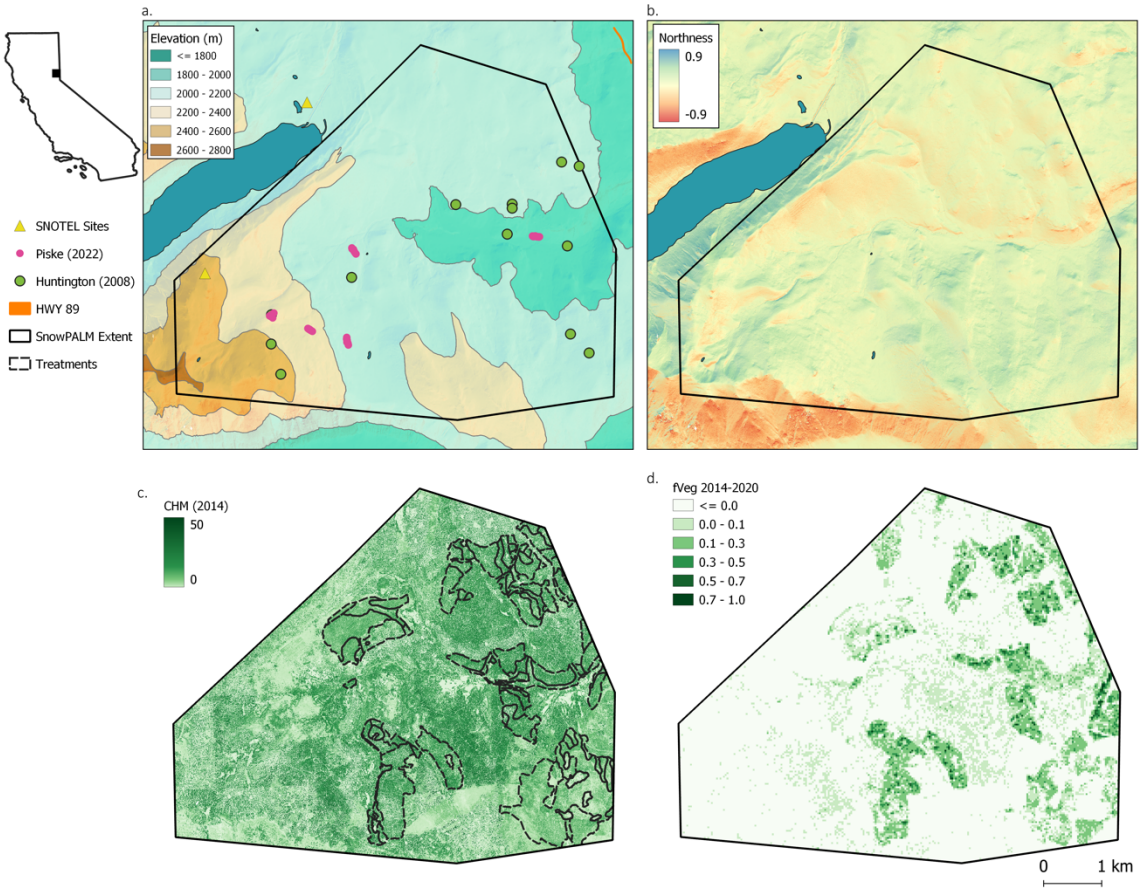

Figure 1. Sagehen Creek Basin, located in the northeastern Sierra Nevada. The area of interest (black outline) shows the study domain given available lidar and modeled density. a. The elevation profile spans ~1800 to 2600 meters, increasing to the southwest (with hillshade). b. Northness shows steep slopes to the southwest. c. The thinning project summary shows proposed thinning boundaries overlaying a canopy height model, which align well with the fVEG difference between the pre- and post-disturbance flights (d).

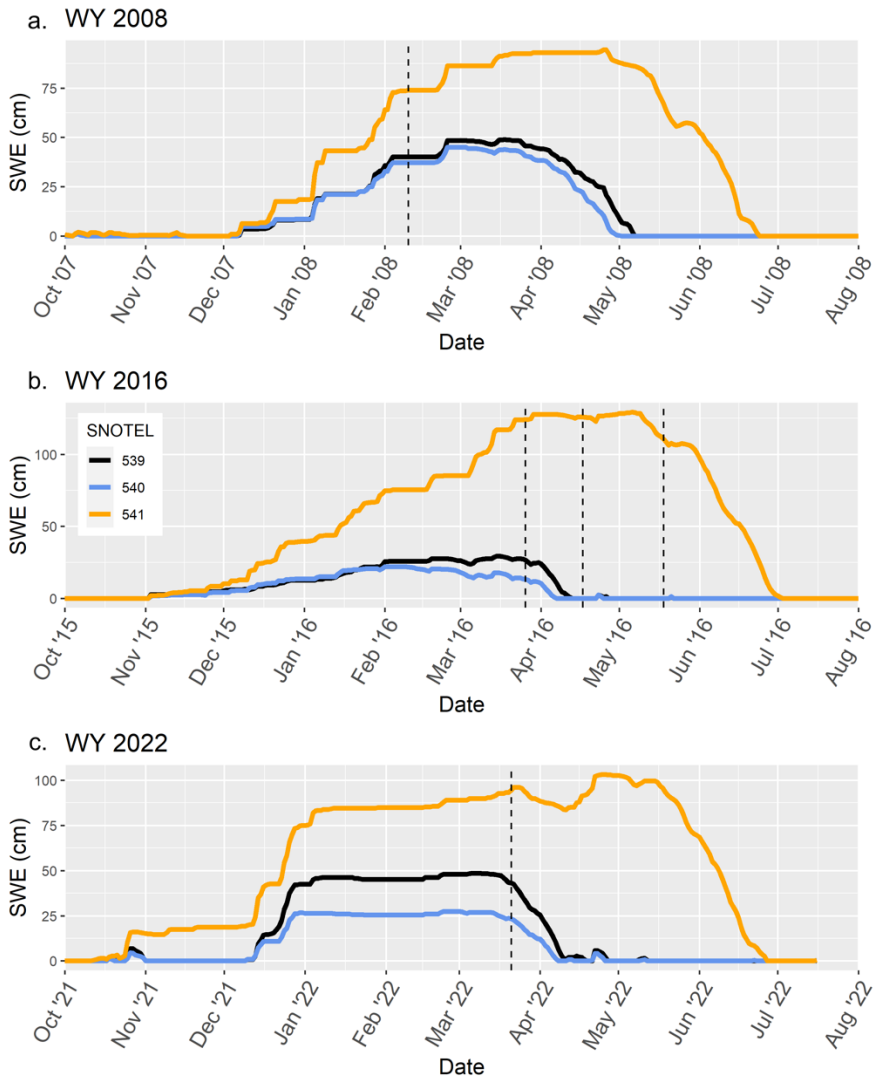

Figure 2. SNOTEL SWE values against flight dates (vertical lines) for the three snow-on years, a. 2008, b. 2016, and c. 2022. Orange = Independence Lake SNOTEL Site (541), Black = Independence Camp SNOTEL Site (539), Blue = Independence Creek SNOTEL Site (540).

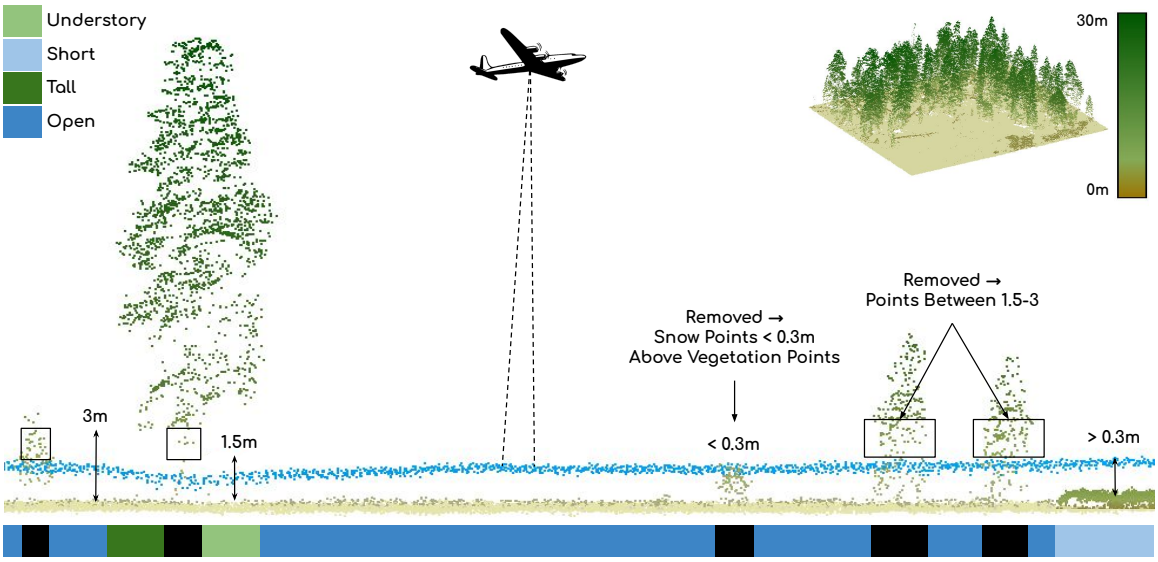

Figure 3. Example image displaying the lidar snow-on classification with an example subsection of a lidar grid cell. The bottom colorbar aligns with the correct canopy cover class as classified from the height strata (dark blue = open, light blue = short canopy, dark green = tall canopy, light green = understory). The black boxes indicates that the area above would be removed from the analysis, either because there are points between 1.5-3 m or because the snow is not >0.3 m above the vegetation surface. (not to scale)

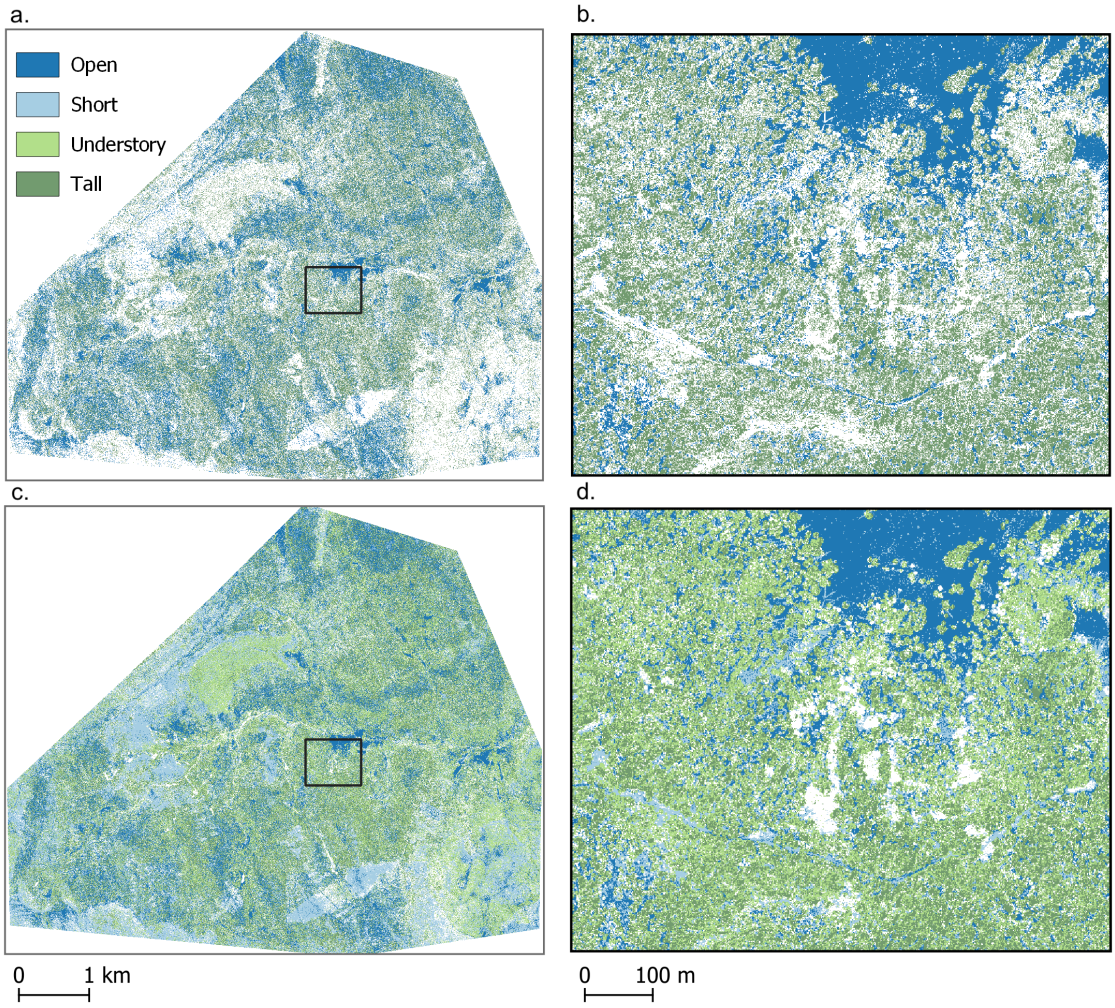

Figure 4. Vegetation classification output comparing Kostadinov et al. (2019) (a. and b.) and our refined classification (c. and d.). While the original classification includes only tall (dark green) and open (dark blue) vegetation classes (a. and b.), the refined classification includes short and understory classes, allowing us to include shorter vegetation types if the snow depth is ≥ 0.3 m above the vegetation (c. and d.).

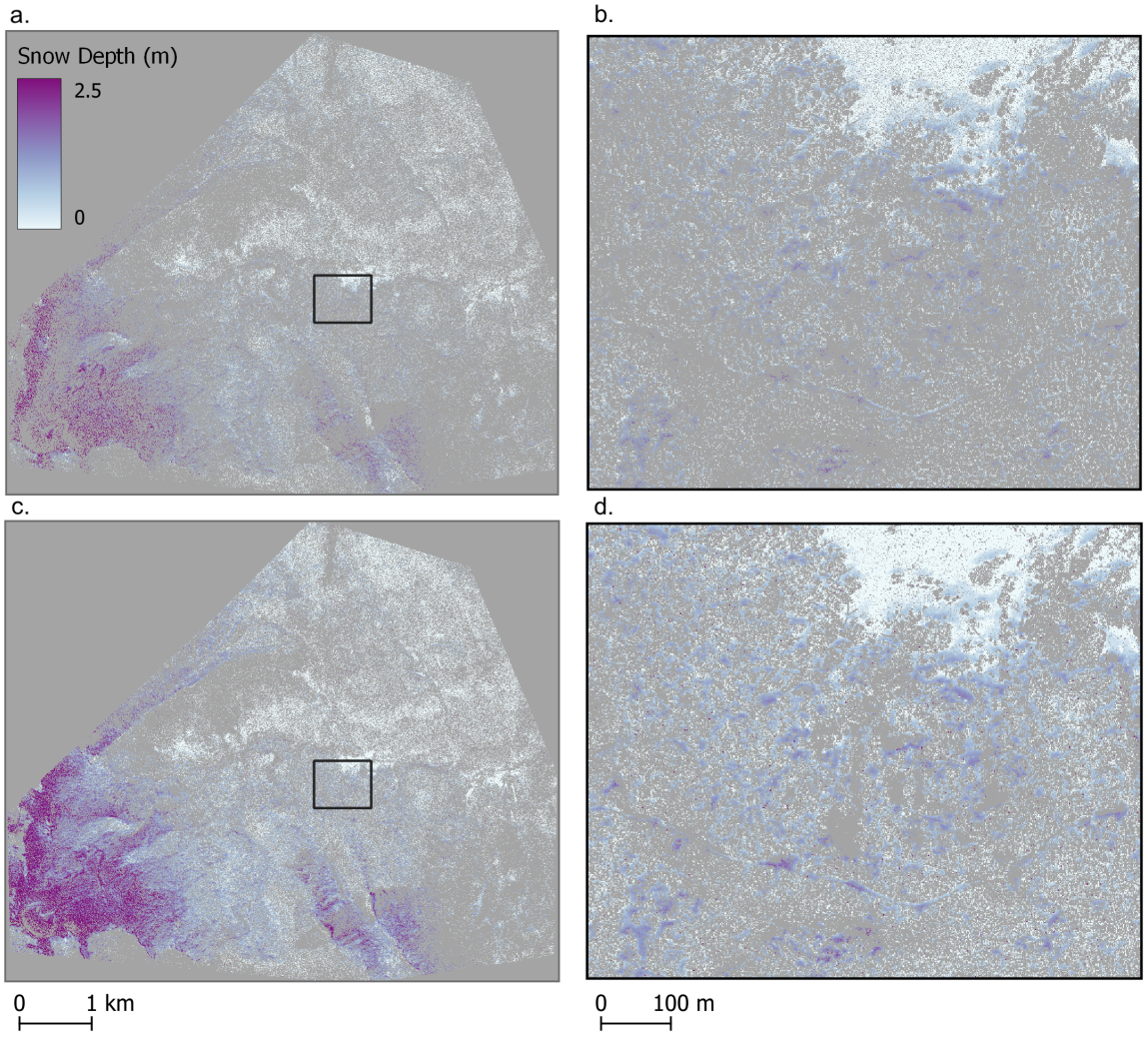

Figure 5. Snow-depth comparison between Kostadinov et al. (2019) (a. and b.) and our results (c. and d.) for the 04/17/2016 flight highlighting the advantages of the refined classification. Our refined classification approach increases the number of valid pixels by including short and understory pixels as potentially valid, if calculated snow depth is ≥0.3 meters above the vegetation.

Snow and Vegetation on the Landscape

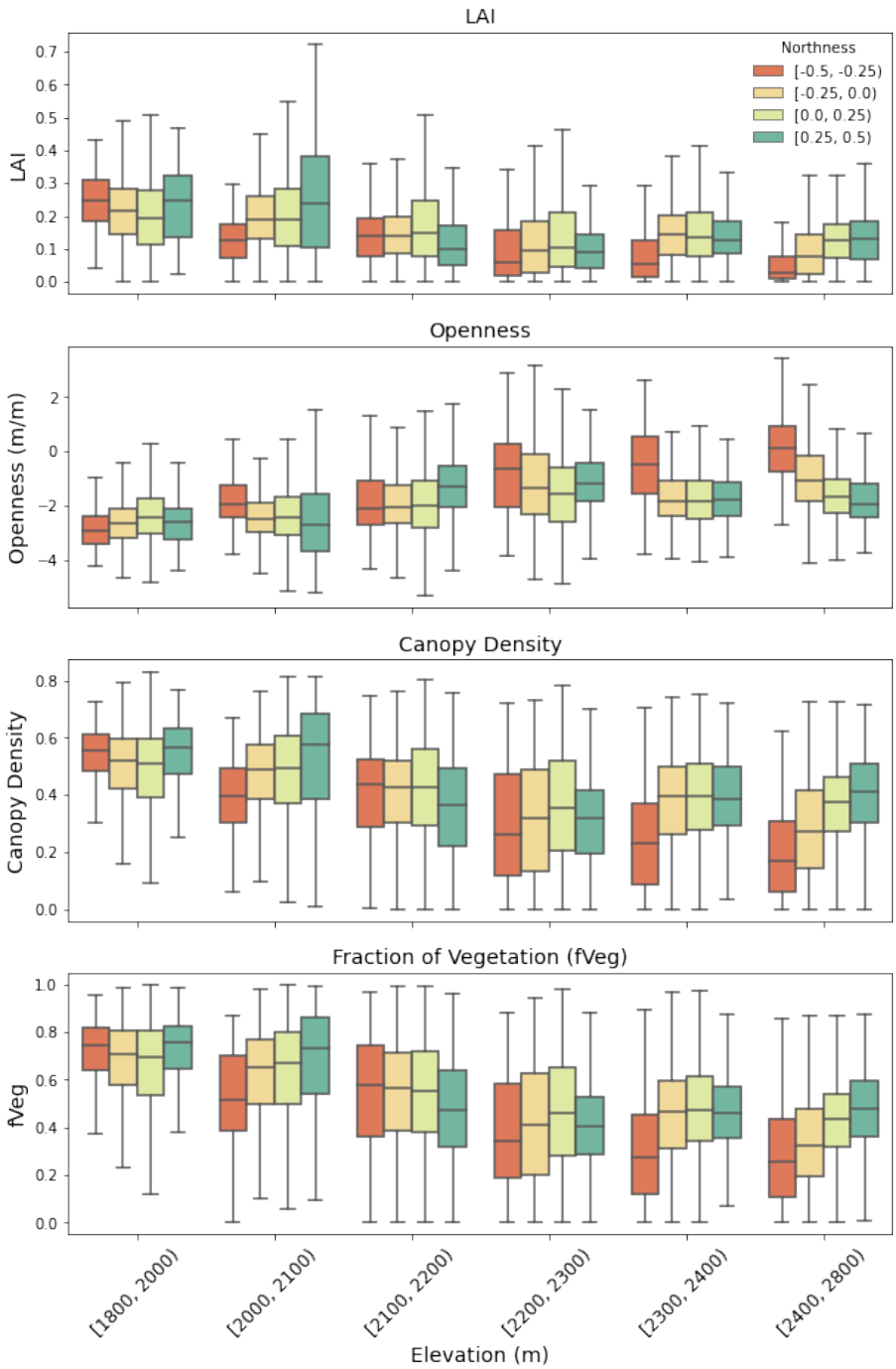

Figure 6. Spatial distribution of pre-disturbance forest structure metrics across the area of interest, colored by northness. Higher elevations see more sense canopy on northern-facing slopes.

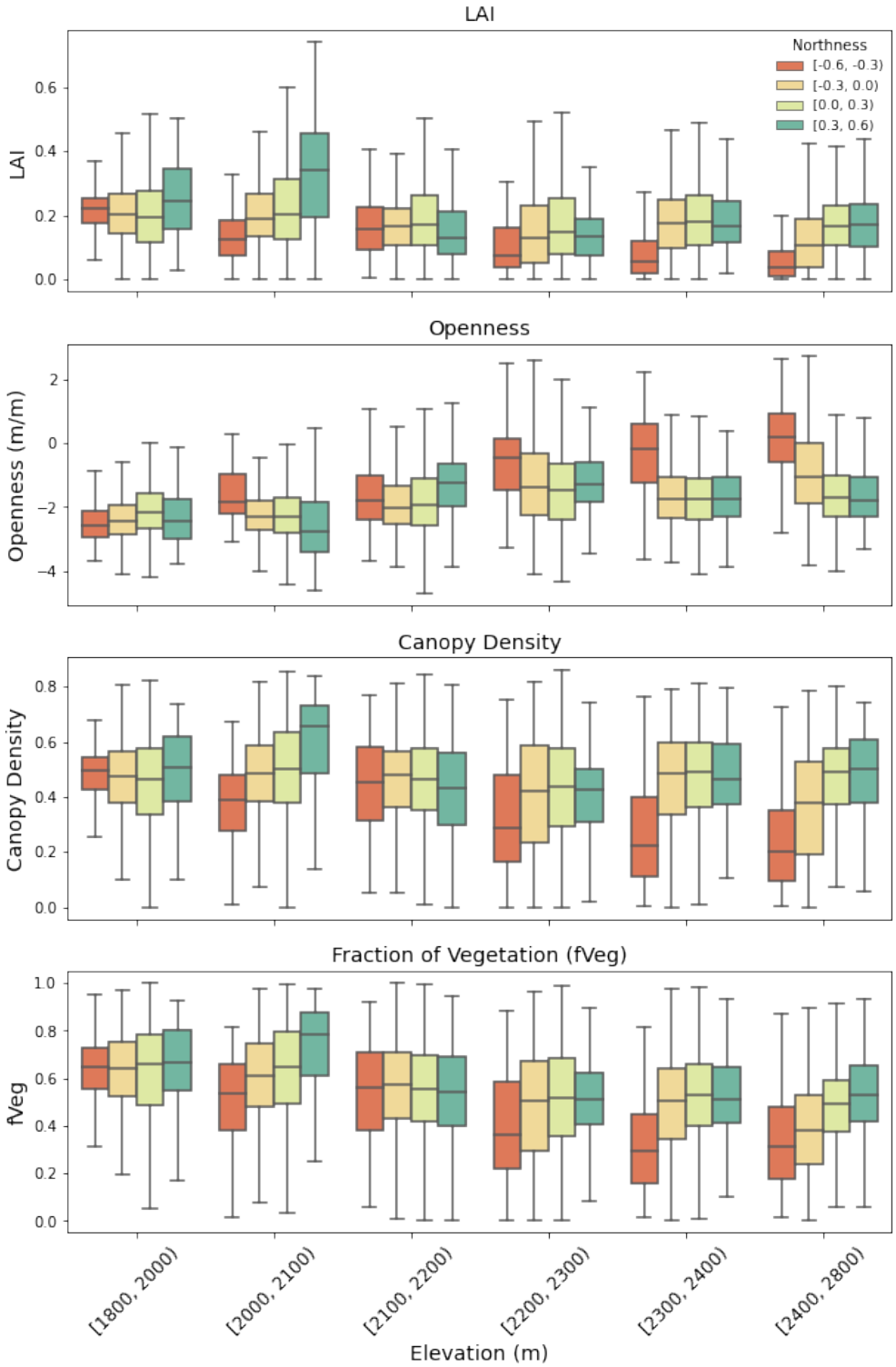

Figure 7. Spatial distribution of post-disturbance forest structure metrics across the area of interest, colored by northness. Compared to the pre-disturbance metrics, openness increases and fVEG, canopy density, and LAI' increase at lower elevation, more southern-facing slopes.

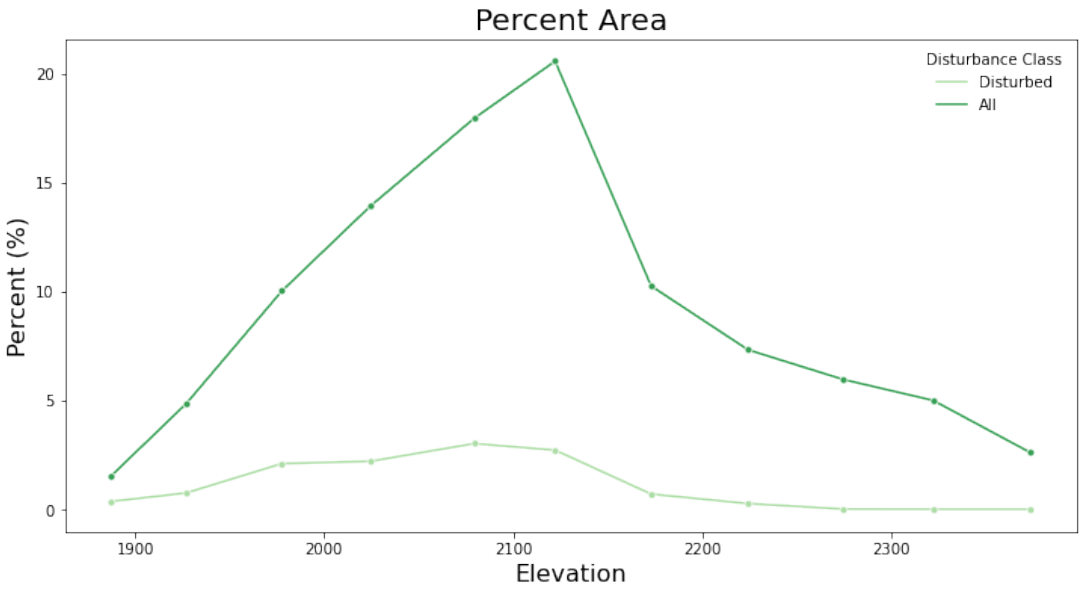

Figure 8. The relative percentage of total area taken up by each elevation bin showing that disturbance primarily occurred below 2400 meters.

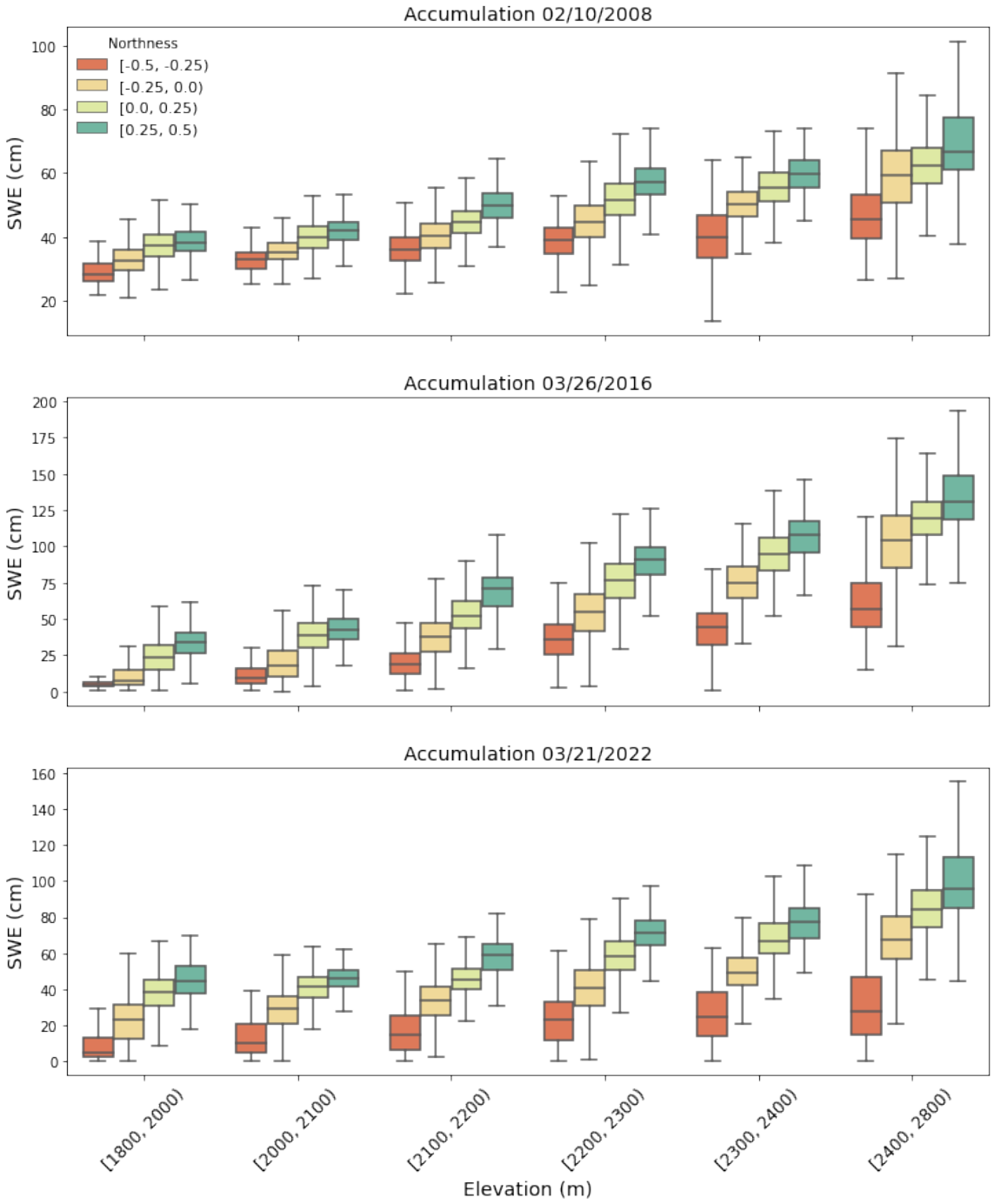

Figure 9. The spatial distribution of SWE across the domain shows greater SWE on higher elevations and more northern-facing slopes.

Delta SWE and Delta Ablation on the Landscape

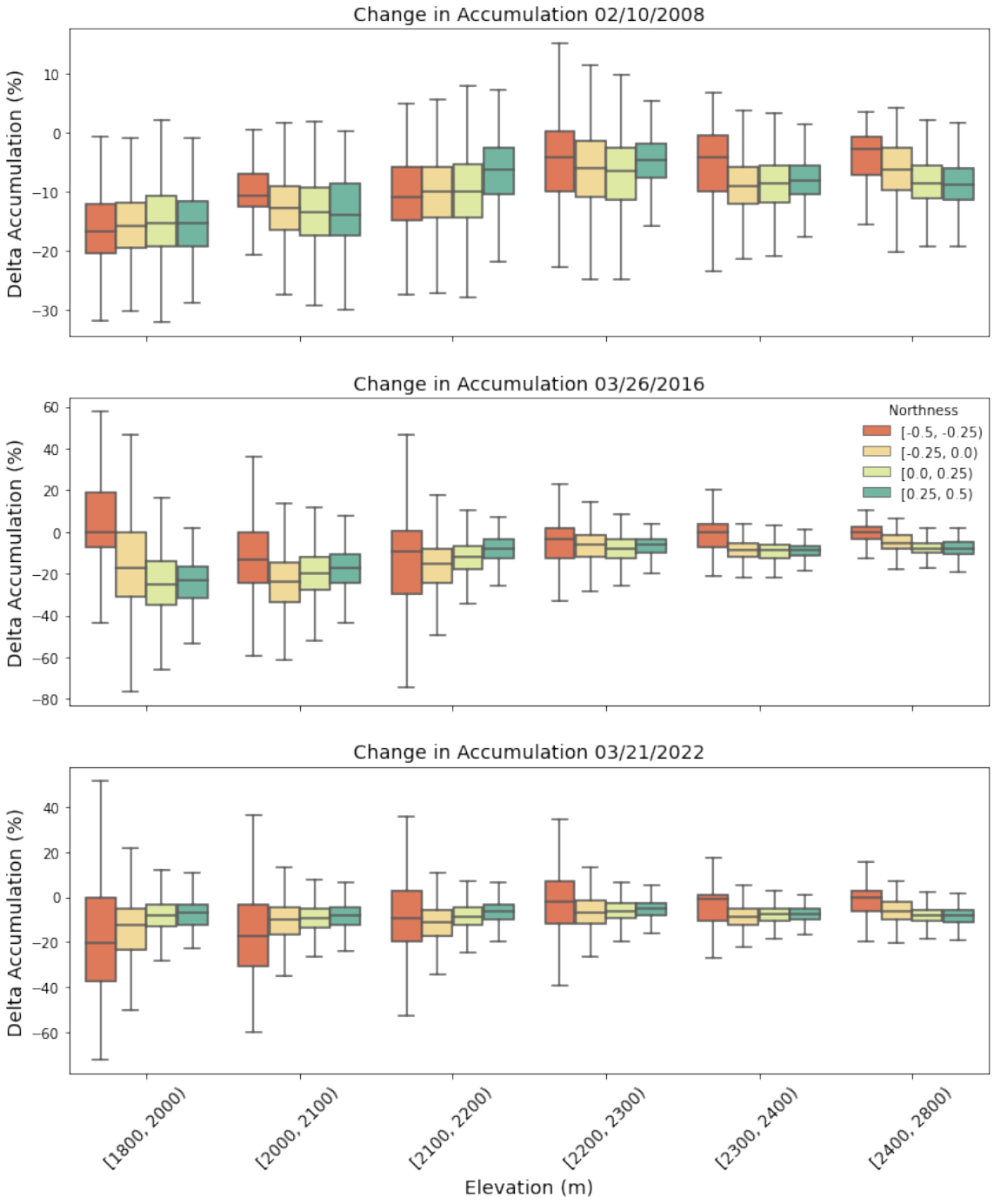

Figure 10. The spatial distribution of delta Accumulation across the domain shows a more drastic difference at lower elevations on more northnern-facing slopes.

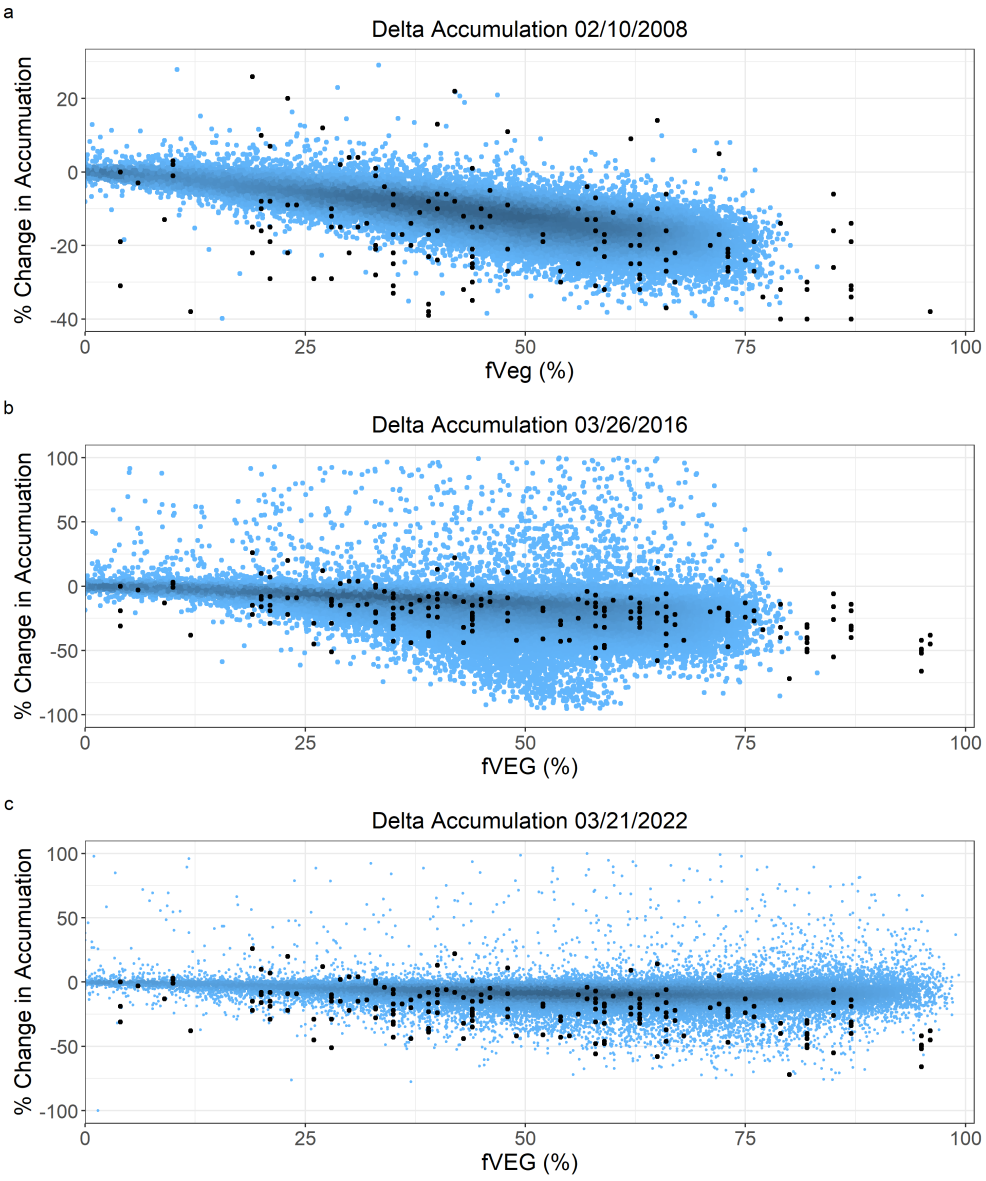

Figure 11. Delta accumulation against fVEG for the a. NCALM flight from 02/10/2008. b. ASO flight from 03/26/2016 c. NCALM flight from 03/21/2022. Lidar points are colored by density with darker blue = greater point density. Black points show the Varhola et al. (2010) data.

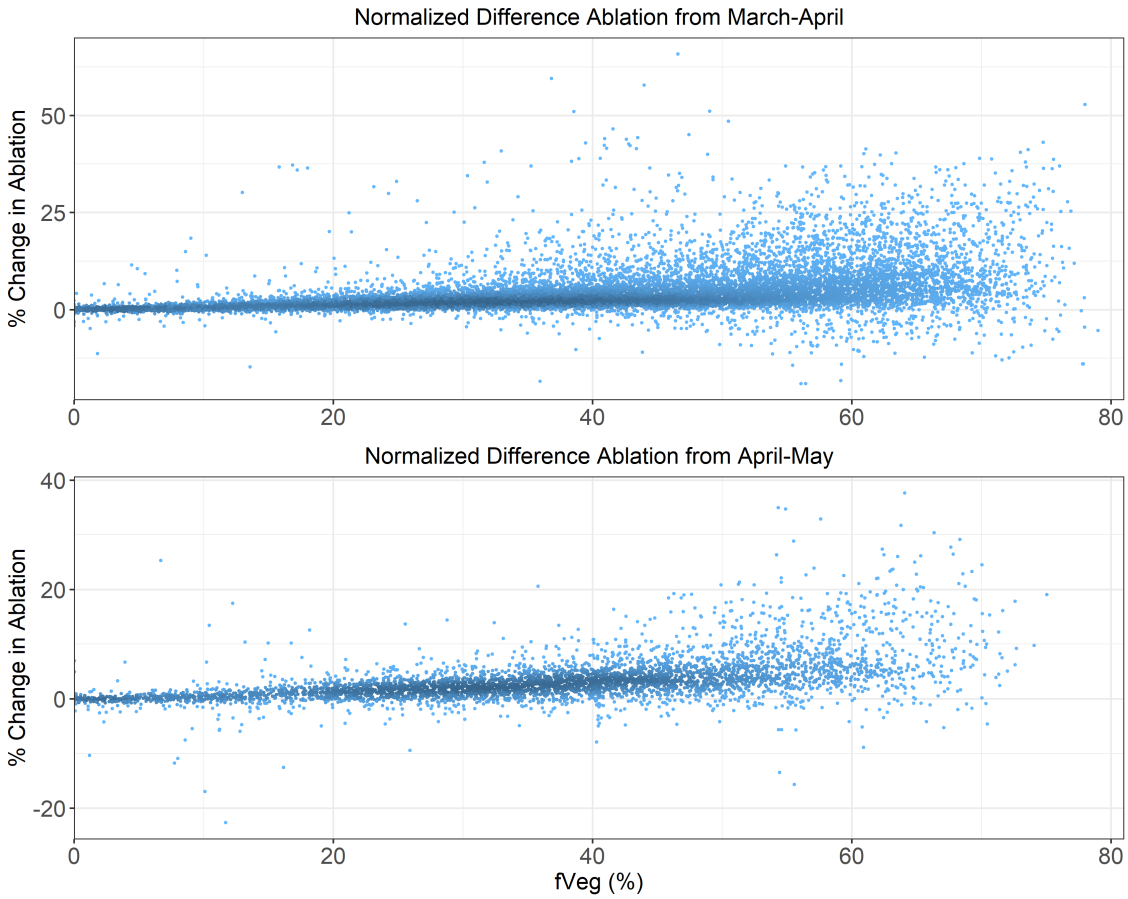

Figure 12. Normalized delta ablation against fVEG for both early (a) and late (b) season ablation show a weak positive relationship, with the differences between forested and open sites increasing (becoming more positive) with increasing vegetation.

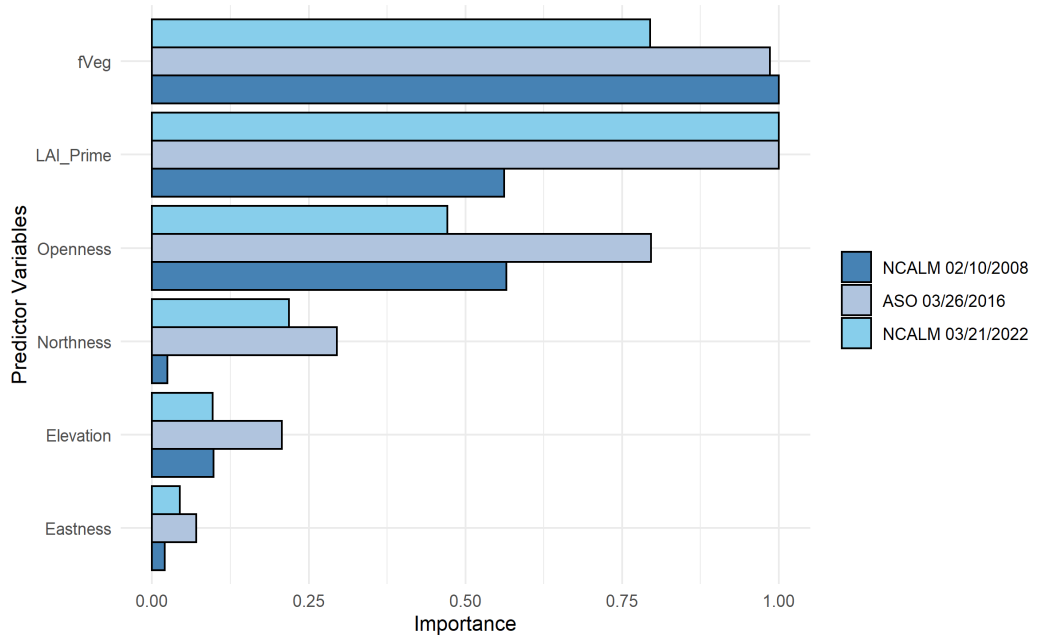

Figure 13. Combined importance plots for the RF model to predict delta accumulation, scaled to the maximum importance factor. The three flights show similar importance trends with fVEG, LAI', and openness emerging as the most important predictor variables.

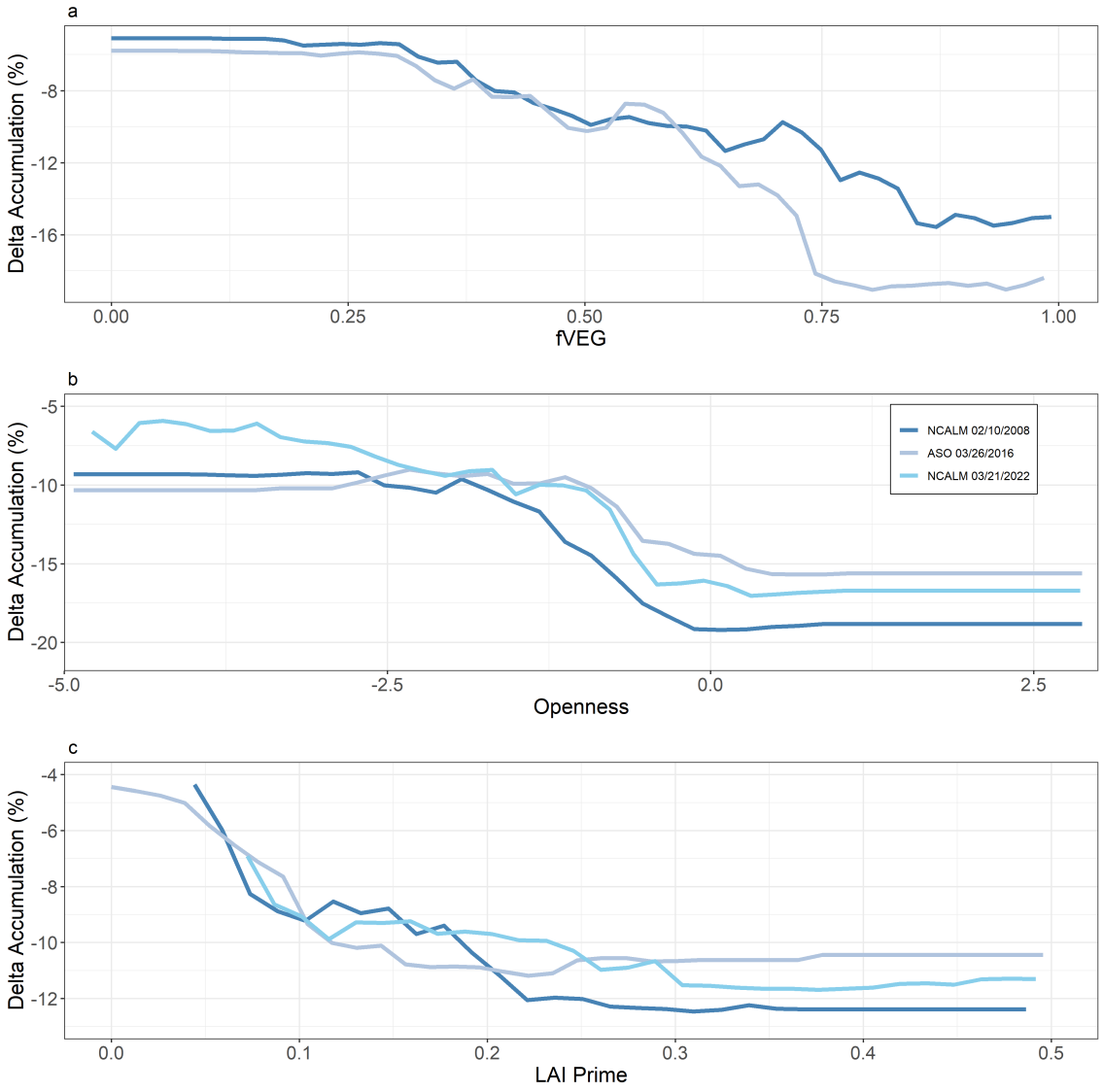

Figure 14. Select partial plots from delta accumulation RF model results showing similar trends in three forest structure metrics: a. fVEG, b. openness, and c. LAI'. Delta accumulation becomes more negative with and increased in all three canopy cover metrics.

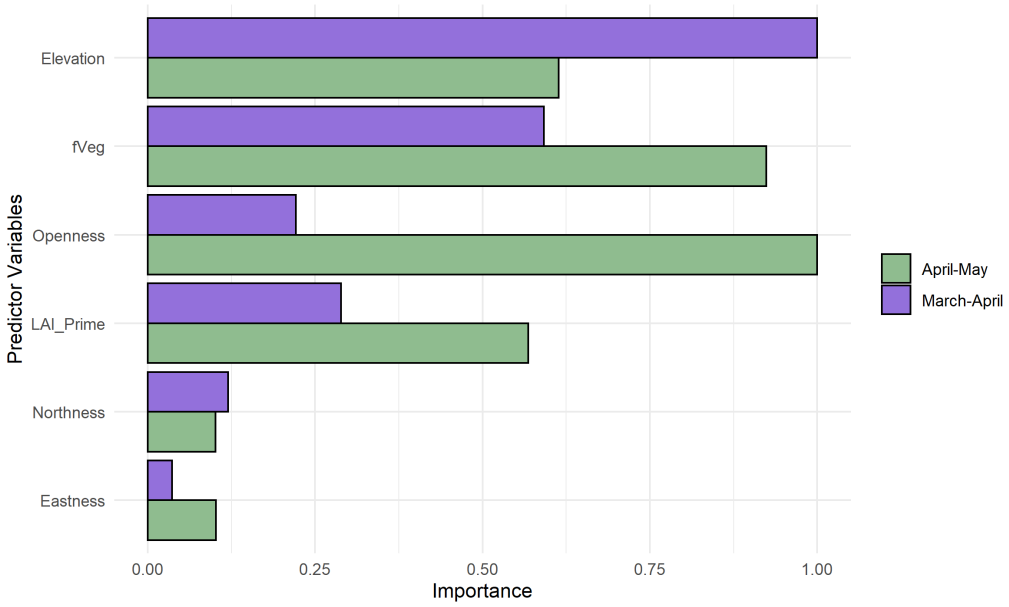

Figure 15. Combined importance plots for the normalized delta ablation RF model, scaled to the maximum importance factor. The results show that early season ablation (March-April) is controlled by elevation and fVEG while later season ablation is controlled by openness and fVEG.

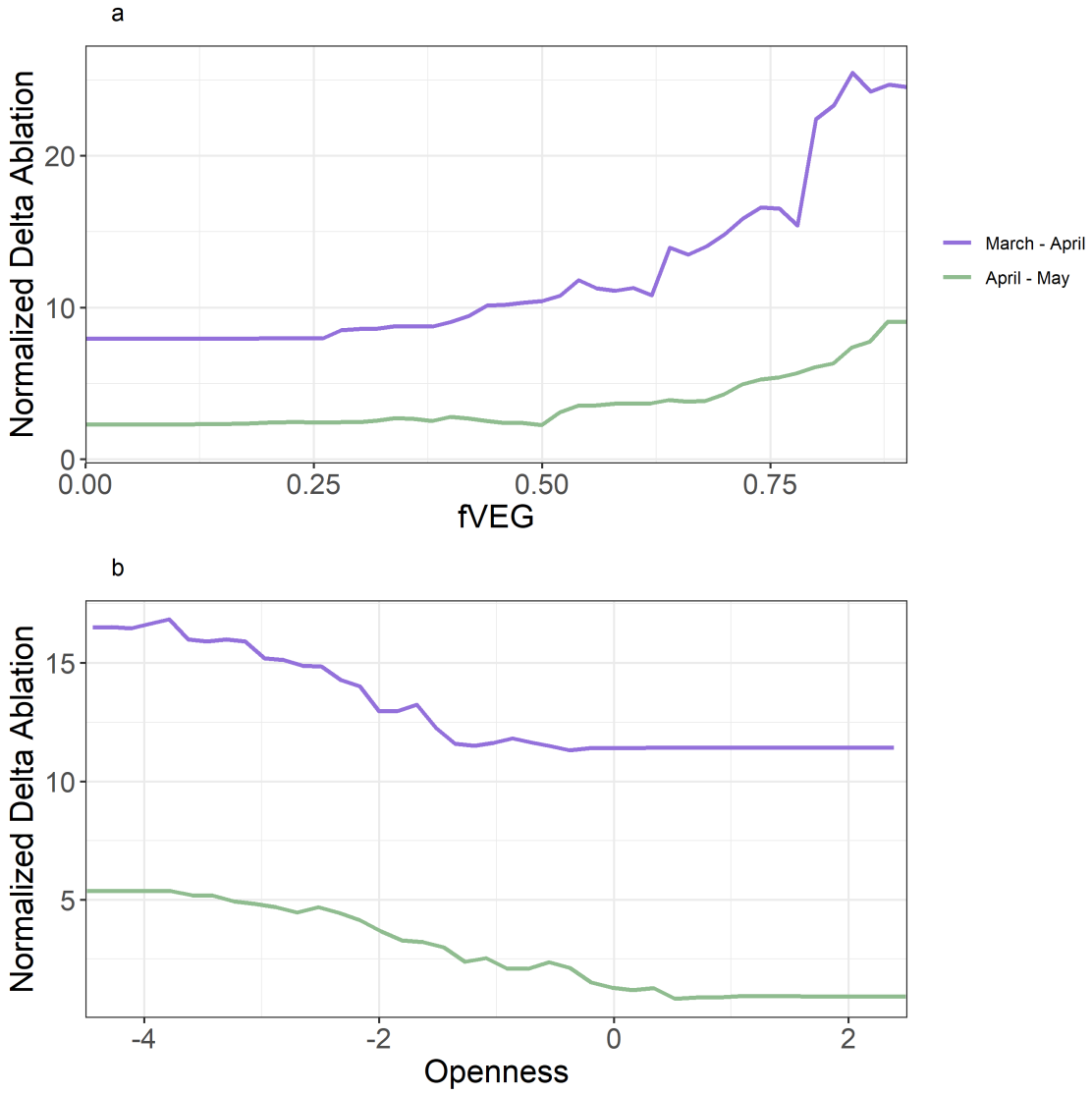

Figure 16. Select partial plots from delta ablation RF model results showing similar trends fVEG (a) and openness (b)

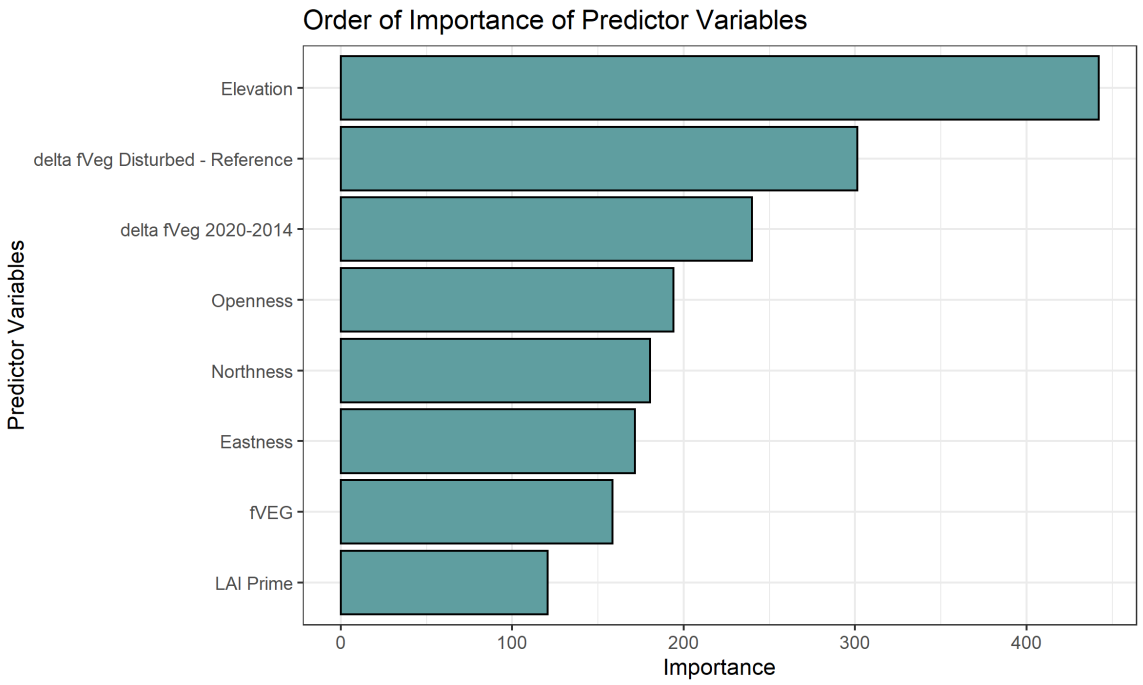

Figure 17. Importance plot for the pre- and post-disturbance RF model using the search algorithm analysis, scaled to the maximum importance factor.

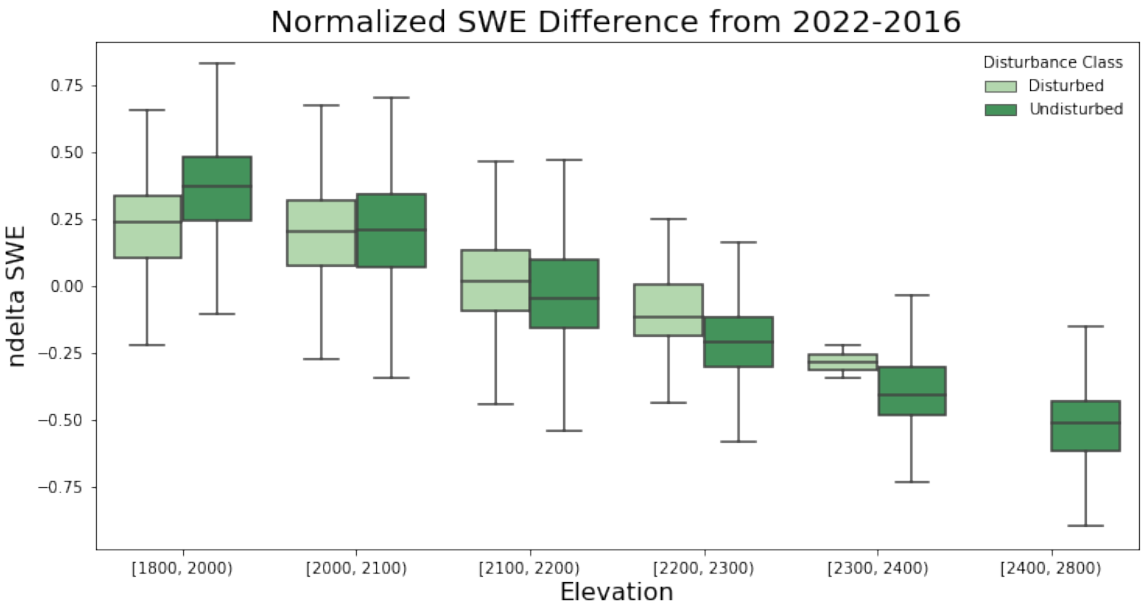

Figure 18. The spatial distribution of the direct-comparison delta-SWE metric across the domain shows higher delta SWE overall in lower elevations, indicating more snow in 2022 relative to 2016. In areas with prominent disturbance (<2,200 m) delta SWE is less in disturbed areas relative to undisturbed areas at the lowest elevations, but delta SWE is greater in disturbed areas relative to undisturbed areas as elevation increases. See Equation 3 for details on delta SWE.

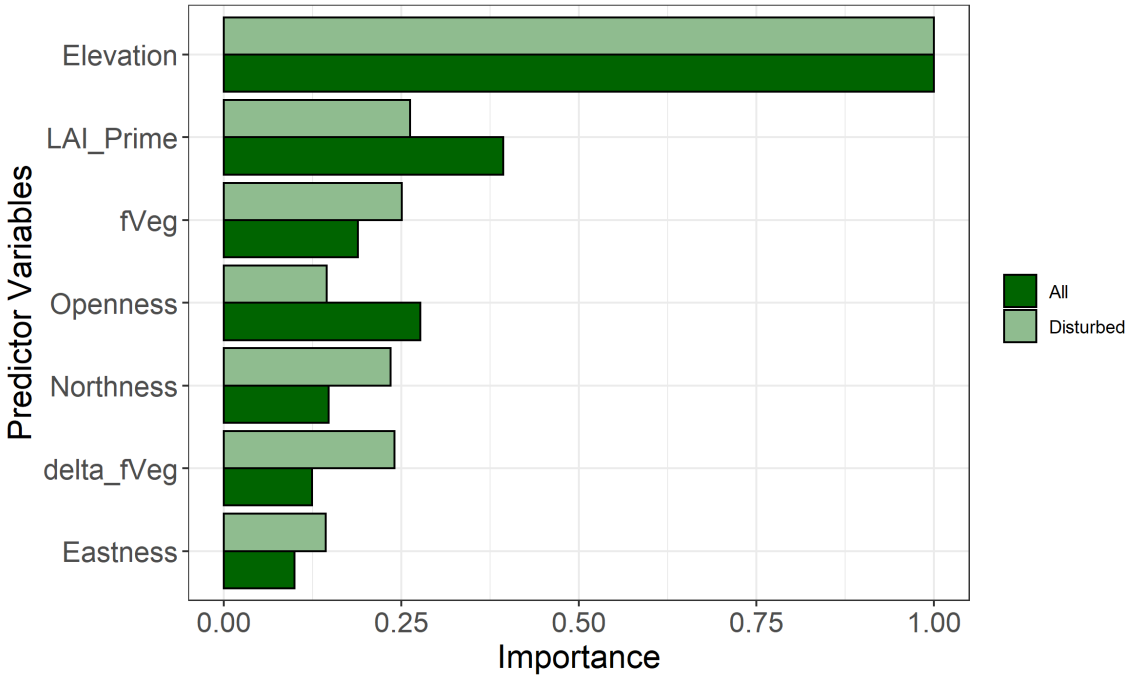

Figure 19. Combined importance plots for the pre-and post-disturbance RF model using the direct comparison analysis, scaled to the maximum importance factor.

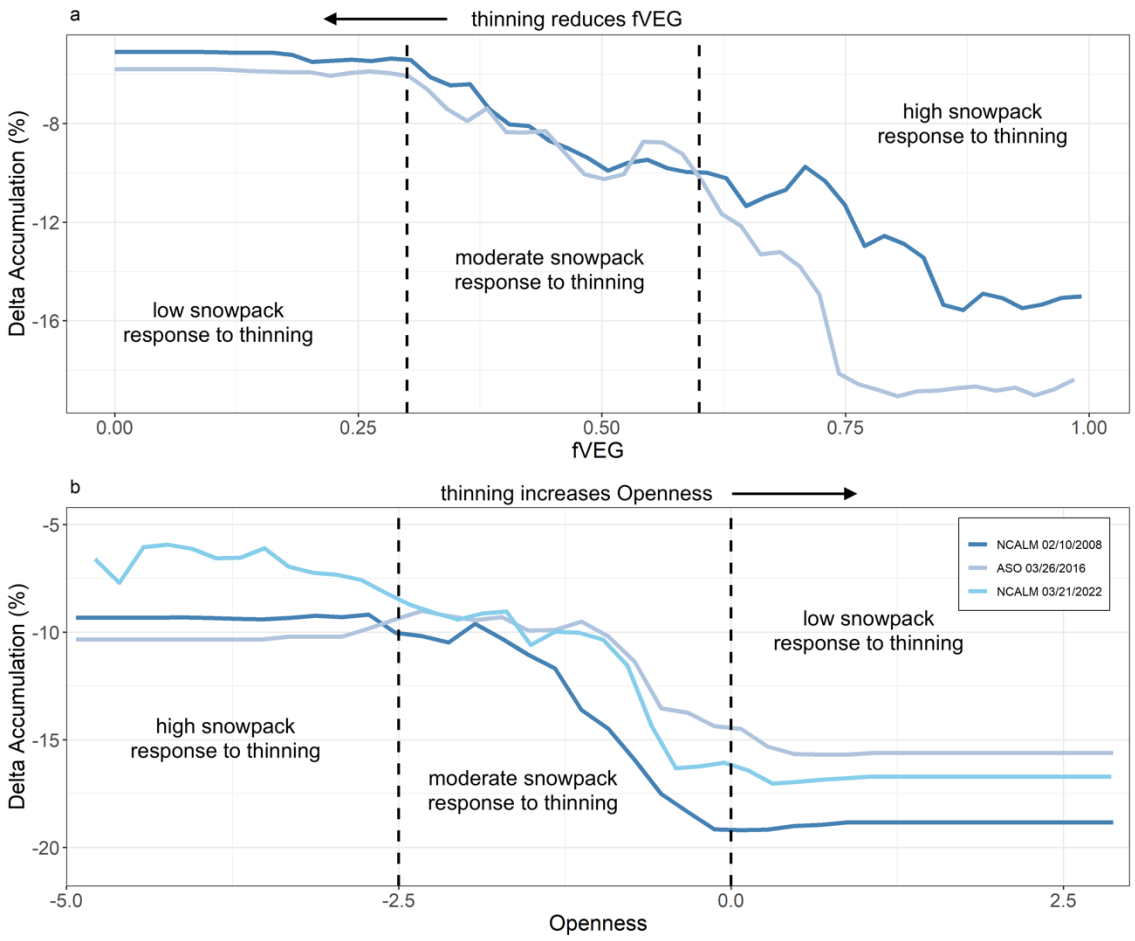

Figure 20. Annotated partial plots showing the response area determination. Higher pre-disturbance fVEG areas are identified as high response areas because thinning would lead to a drastic increase (positive response) in delta accumulation whereas lower pre-disturbance Openness areas are identified as high response because thinning would lead to a drastic decrease (negative response) in delta accumulation.

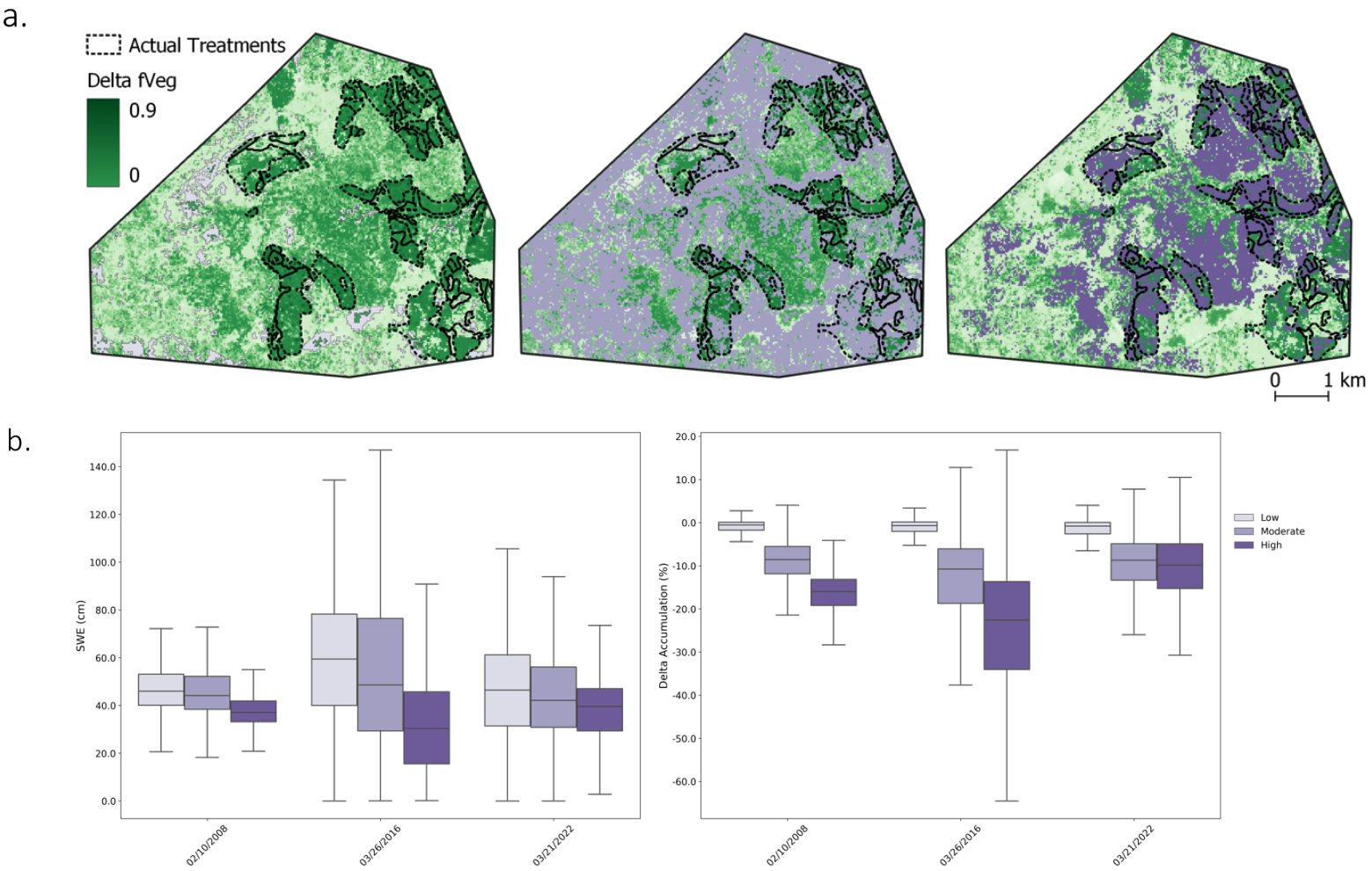

Figure 21. Predicted response classes based on the RF results. Shading shows areas that are predicted to experience a low (light purple), moderate, or high (dark purple) response to treatment. a. The spatial distribution of these maps on top of actual treatments, shown both as planned treatment outline (dotted black line) and the delta fVEG raster. b. Snow accumulation dynamics across all three flights and predicted response classes.

Appendix A

Lidar Processing

All NCALM flights can be found on OpenTopography (https://portal.opentopography.org/datasets). ASO flight data was supplied directly from the vendor. The ASO flight data is pre-processed using the Riegl RiPROCESS software and the NCALM data is pre-processed using the TerraSolid software (https://terrasolid.com/products/terrascan/). Once pre-processed, point clouds are provided, which is where the processing for this project began.

After retiling the data into 1000x1000 m tiles (with a 50 m buffer) and renaming to match consistent naming structures, the first step in pre-processing was to reproject all data into a consistent vertical datum. NASA's VDATUM software was used for this process. All data was reprojected into the NAD83 horizontal and NAD83 vertical coordinate reference system (epoch 2010; EPSG: 6339). The data were then pre-processed to exclude slopes >30° (Tinkham et al., 2014)and all water bodies were removed (based on delineations from the National Hydrography Dataset, https://nhd.usgs. gov/).

Point-cloud processing was performed in Python using PDAL (Butler et al., 2020). DEMs were created using PDAL's rasterization filter, which applies the specified function (e.g., mean) to all points within a specified search radius. DEMs were created using a search radius of 1 meter with a window size of 3 m to give us a wall-to-wall product. All other rasters were created using the default. Height above ground was determined using a point-raster differencing.

For vertical bias corrections, a search radius was determined by investigating data distribution around a coordinate to determine which radius was the most representative of

surrounding snow depth (Figure A2). A radius of 3 was chosen to maximize representative points while minimizing computation time.

Height strata were calculated from the corrected point-clouds, with slight modifications from Kostadinov et al., 2019 (See Table A1). The refined classifications allowed us to broaden the search for snow-covered pixels beyond tall forests into shorter canopy, which has found to influence radiative transfer models and energy balance under the canopy (Figure 5) (Webster et al., 2020). Open pixels were defined only using the presence of returns within uncertainty of ground (+/- 0.15 m). This number is based on previous values cited in the literature and confirmed using the variance around bias-corrected values (the 5th-95th percentile range) (Kostadinov et al., 2019). Tall vegetation was classified as only pixels containing tall forests without low branches or underlying vegetation. Understory encompasses low-lying branches or underlying vegetation beneath treetops. It cannot represent a medium sized tree, for example. Short vegetation contains low-lying returns with no overhead canopy. In addition, an open-reference pixel is classified as an open pixel at least one meter from the nearest canopy-classified (tall or understory) pixel (Figure A3).

All final vegetation classifications were created using a series of raster calculations using the GDAL library (GDAL/OGR contributors, 2020). From the lidar files, we extracted the number of returns in each height strata in Table A1. The rasterized product was used to create logical rasters representing the different conditions in Table A1.

For example, to classify pixels as open, we started with a raster that contained the number of returns (counts or NOR) between -0.15-0.15 m. A logical raster was created, representing whether a pixel can be passed to the next filtering step for the open

classification. This raster has values of 1 (True) for pixels that contain returns between -0.15-0.15 m and a value of 0 for pixel that do not (False).

Example: Understory pixel classification

1. Vegetation height strata rasters [each pixel = NOR]
    a. NOR [-0.15-0.15)
    b. NOR [0.15-1.5)
    c. NOR [1.5-3)
    d. NOR [3:)
1. Intermediate logical rasters [each pixel = binary, 1-True, 0-False]
    a. NOR [-0.15-0.15) >= 0
    b. NOR [0.15-1.5) > 0
    c. NOR [1.5-3) == 0
    d. NOR [3:) > 0
1. Final logical raster [each pixel = binary 1-Understory, 0-NaN]
    a. a*b*c*d above

For understory and short pixels, it is necessary to also extract the height of the vegetation for further filtering. Simply multiply the final logical rasters from above with a CHM created using only points <= 1.5 m.

Canopy structure metrics were primarily created from raster products using GDAL; however, the CHM was calculated from the raw point clouds using the maximum value in each pixel, and TAOs were created from the lidR package (Dalponte & Coomes, 2016; J. Roussel & Auty, n.d.; J.-R. Roussel et al., 2020).

Snow depth was calculated over the pixels filtered into the four vegetation height strata (tall, understory, short, open). Based on maximum depth heights from the recorded SNOTEL record, 5 meters was chosen as the maximum snow depth in the open areas. Due to the 3-meter cutoff for tall vegetation, 3 meters was chosen as the maximums now depth under the canopy. Short and understory pixels were classified as snow if the calculated depth

was at least 0.3 meters above the vegetation surface. This value was chosen as a conservative estimated based on a +/- 0.15m vertical uncertainty in the of the lidar data.

Data and Analysis Errors

See Table A4 for a detailed overview of instrumentation and horizontal and vertical accuracies of each lidar dataset. Error is governed by several sources including acquisition instrumentation (e.g., inertial measurement unit (IMU) and global positioning systems (GPS) calibrations), terrain, and vegetation. See Deems et al., 2013 for more details. Lidar strength is weakened as it interacts with canopy, decreasing the number of returns that reach the ground. Previous work has shown that there is more variability in under canopy returns, in addition to less GPS accuracy (Deems et al., 2013; Hopkins et al., 2004; Tinkham et al., 2014). Kostadinov et al. (2019) showed that there was no detectable SWE bias when increasing grid size due to point density losses under the canopy for the 2016 data. These data are particularly vulnerable to data sparsity bias because of the low point density. The two snow-on NCALM flights have greater point density, so these impacts would be expected to decrease. We attempted to account for these biases using a weighting parameter in the RF analysis but found no difference in the model skill or defined importance. This parameter should be investigated further in the future to better account for data sparsity bias.

In addition, the RF model itself can be impacted by dimensionality and spatial autocorrelation. We did not perform filtering to reduce the number of non-relevant features in our analyses (Belgiu & Drăgu, 2016). A sensitivity analysis was performed on each RF model (e.g., Figure A17) to confirm model skill.

Figures and Tables

Table A1: Refined Vegetation Classification Logic

Strata Intervals	**Number of returns ∈ [-0.15,0.15) m**	**Number of returns ∈ [0.15,1.5) m**	**Number of returns ∈ [1.5,3) m**	**Number of returns ∈ [3.00, +∞) m**
Open	∈ (0, +∞)	0	0	0
Tall Veg	∈ [0, +∞)	0	0	∈ (0, +∞)
Short Veg	∈ [0, +∞)	∈ (0, +∞)	0	0
Understory	∈ [0, +∞)	∈ (0, +∞)	0	∈ (0, +∞)

Note: Short vegetation includes shrub/grass etc. found in the open, understory includes low branches/shrubs/grasses/etc. found under taller canopy. Modified from Kostadinov et al., 2019 (Supplement Figs. S1 and S2).

Table A2: Refined Snow Classification Logic

Snow-on pixel classified as:	**Snow**	**No snow**
Snow-off open pixel NO short veg	Snow-on HAG ∈ [0.15, 5.00] m	Snow-on HAG ∈ [-0.30, 0.15) m
Snow-off open pixel YES short veg	Snow-on HAG ∈ [x, 5.00] m	Snow-on HAG ∈ [-0.30, 0.15) m
Snow-off tall canopy pixel NO understory	Snow-on HAG ∈ [0.15, 3.00) m	Snow-on HAG ∈ [-0.30, 0.15) m
Snow-off tall canopy pixel YES understory	Snow-on HAG ∈ [x, 3) m	Snow-on HAG ∈ [-0.30, 0.15) m

Note: HAG – height above ground; x – snow-off HAG +0.3.
Short vegetation includes shrub/grass etc. found in the open, understory includes low branches/shrubs/grasses/etc. found under taller canopy. Modified from Kostadinov et al., 2019 (Supplement Figs. S1 and S2).

Table A3: Canopy Structure Metrics

Canopy Cover Metric	Calculation	Source
Canopy Density (CD)	$\frac{Number\ of\ Returns\ >\ 3m}{Total\ Number\ of\ Returns}$	Krogh et al., 2020
Fraction of Vegetation (fVEG) 30m product only	$\frac{canopy\ height\ (where\ canopy\ height > 3\ m)}{grid\ cell\ area\ (900\ m^2)}$	Also called canopy cover fraction; Mazzotti et al., 2019, 2020
Tree Approximate Object (TAO)	local maxima filtering	Dalponte & Coomes, 2016
LAI'	$\frac{canopy\ density\ (CD) * canopy\ height}{\max tree\ height}$	Krogh et al., 2020
Distance to Nearest Canopy (DNC)	Minimum distance from pixel (center) to nearest canopy pixel (center)	Currier & Lundquist, 2018; Mazzotti et al., 2019
Openness Index	$\log\left(\frac{distance\ to\ nearest\ canopy\ (DNC)\ * 2}{avg.tree\ approximate\ object\ height}\right)$ openness < 0 = gap width : canopy height < 1 openness > 0 = gap width : canopy height > 1	Ellis et al., 2013; Musselman et al., 2015
Open-Reference Class	Distance to nearest canopy with 1-m buffer around canopy	Currier & Lundquist, 2018

Table A4: Summary of Lidar Specifications

	NCALM 2008[1]	NCALM 2014[2]	ASO 2016[3]	NCALM 2020[4]	NCALM 2022[5]
Equipment	Optech GEMINI Airborne Laser Terrain Mapper (ALTM) (06SEN195)	Optech GEMINI Airborne Laser Terrain Mapper (ALTM) (06SEN195)	Riegl Q1560	Optech Titan (14SEN340)	RIEGL VQ-580 II (H2225798)
Horizontal Accuracy	1/11,000 x altitude; ±1-sigma	1/5,500 x altitude (m AGL); ±1-sigma		1/7,500 × altitude; ±1-sigma	<= 5 cm
Vertical Accuracy	5 - 10 cm typical; ±1-sigma	5 - 35 cm typical; ±1-sigma	5 – 30 cm	< 5 - 10 cm typical; ±1-sigma	<= 10 cm
Pulse Rate Frequency	33 - 167 kHz	33 - 167 kHz	100-800 kHz	100 kHz	600 kH
Laser Wavelength	1047 nanometers	1064 nanometers	1064 nanometers	1064 nanometers (multi-wavelength)	NIR
Scan Angle	0 to 25°; increments of ±1 degree	0 – 50°; in increments of ±1degree	0 – 60°	± 30°	±37.5°
Scan Frequency	Variable to 100 Hz	0 – 70 Hz		26 Hz	LPS: 200/s
Beam Divergence	Dual Divergence 0.25 mrad or 0.80 mrad	Dual Divergence 0.25 mrad (1/e) or 0.80 mrad (1/e)	<= 0.25 mrad	Dual Divergence 0.35 mrad (1/e) or 0.70 mrad (1/e	0.25 mrad

Notes: Data sources include Huntington, 2008 (1), Guo, 2014 (2), Painter et al., 2016 (3), Graup, 2021(4), and Piske, 2022 (5)

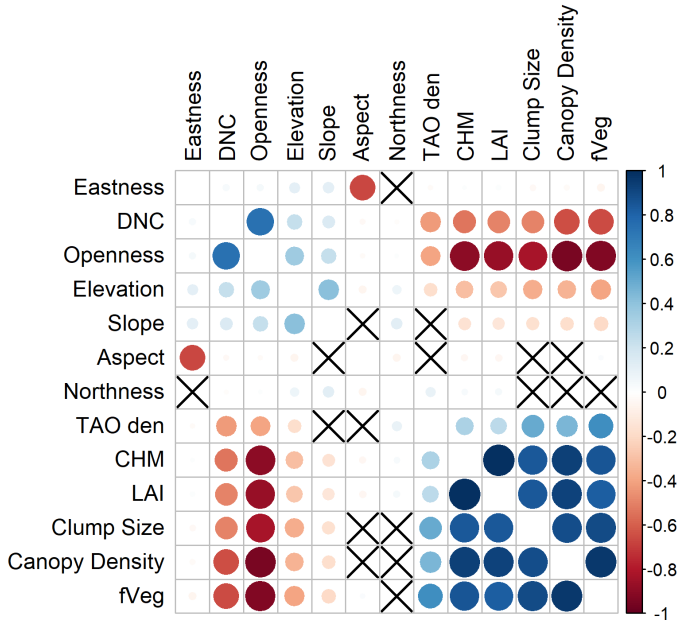

Figure A1. Correlation matrix of terrain and vegetation variables showing that vegetation density metrics, including fVEG, LAI', and Canopy Density are highly correlated. X's represent non-significant correlations.

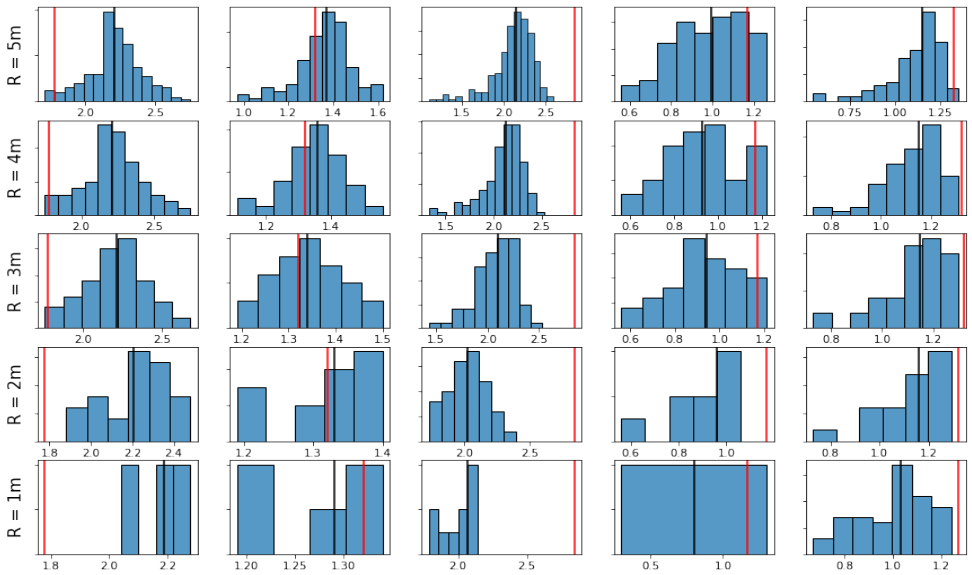

Figure A2. Example vertical bias corrections using different search radii (R) around the ground observation. Red lines show the ground point observation. Black lines show the median values of lidar points within each search radius. The median difference between the black and red lines with a 3-m search radius was used for the vertical bias correction.

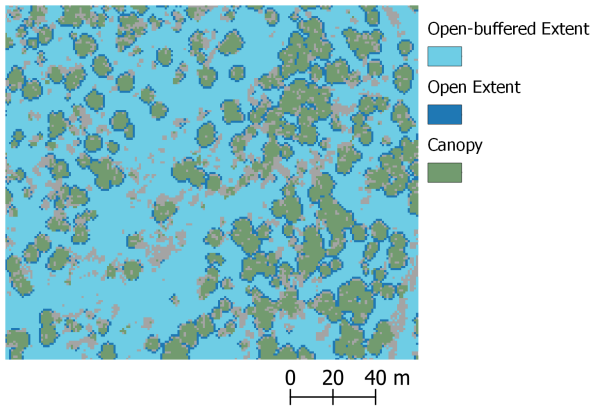

Figure A3. Visual representation of the open-reference pixel classification. Light blue areas indicate pixels that were classified as open-reference. Underlying dark blue shows the extent of the regular open pixels. Green shows canopy or understory. Grey areas represent no-data pixels.

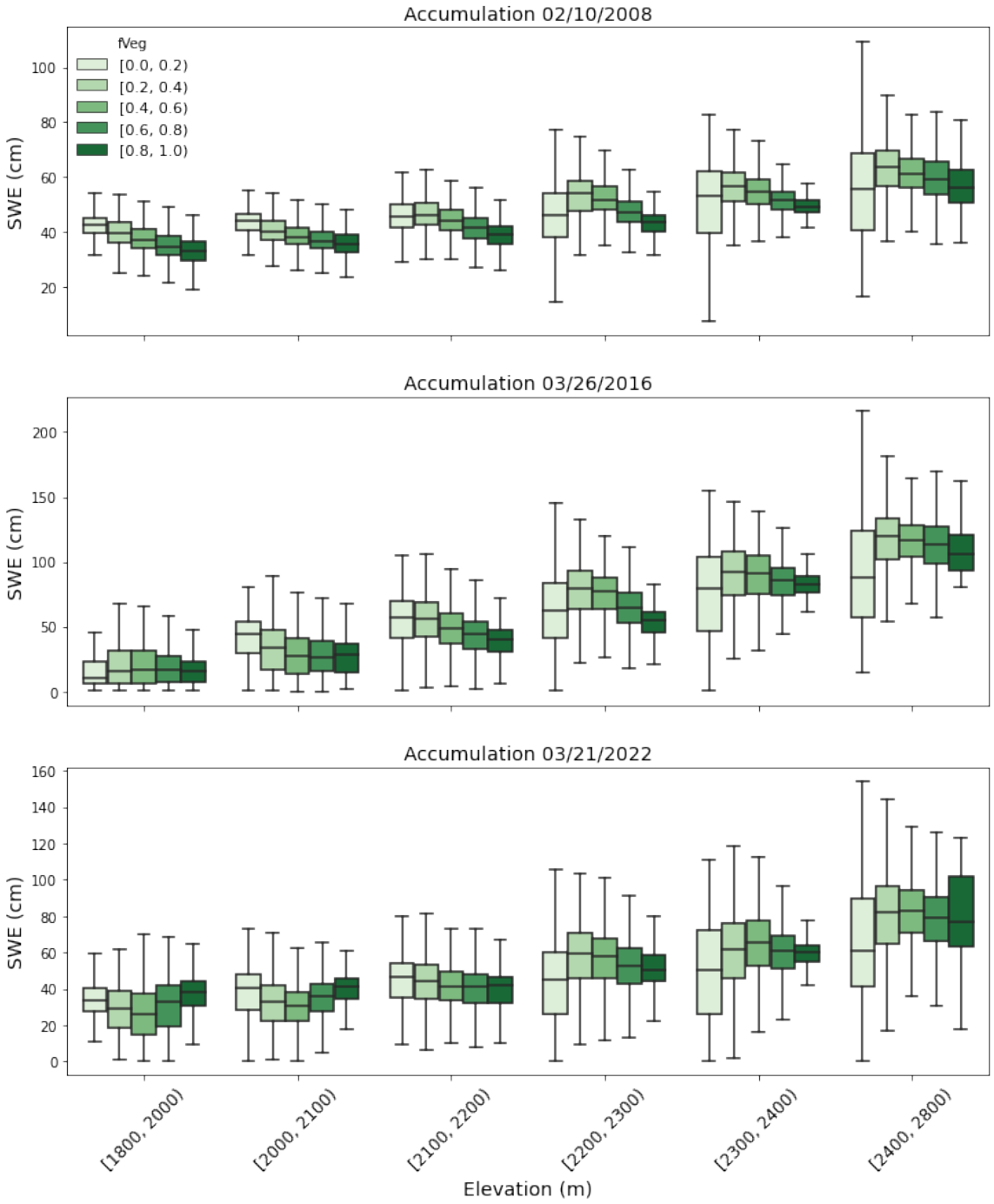

Figure A4. The distribution of SWE across the domain shows increased SWE with increasing elevations but decreasing fVEG, with more varied low-elevation trends post-disturbance.

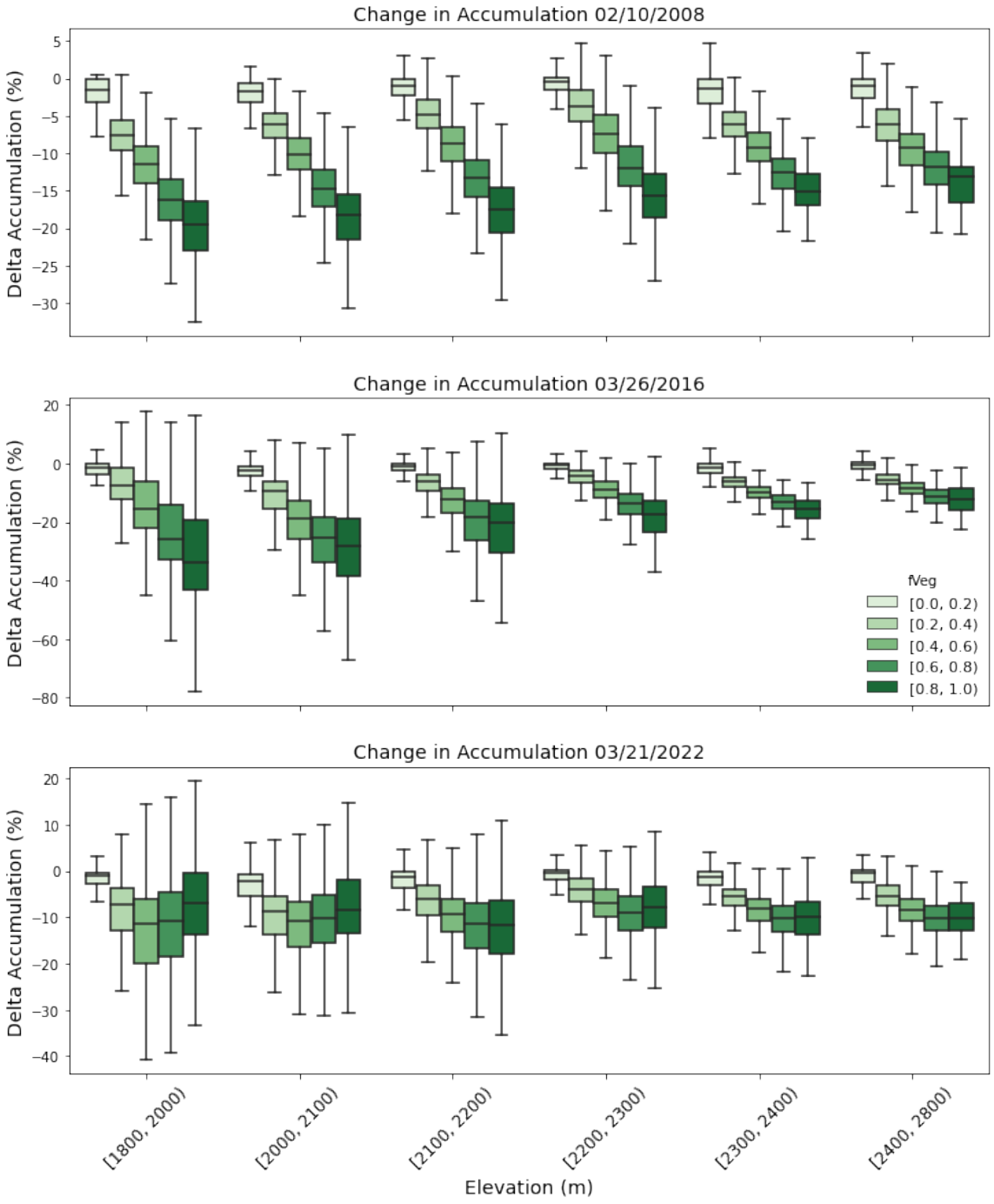

Figure A5. The spatial distribution of delta Accumulation across the domain shows a more drastic difference at lower elevations with increasing fVEG.

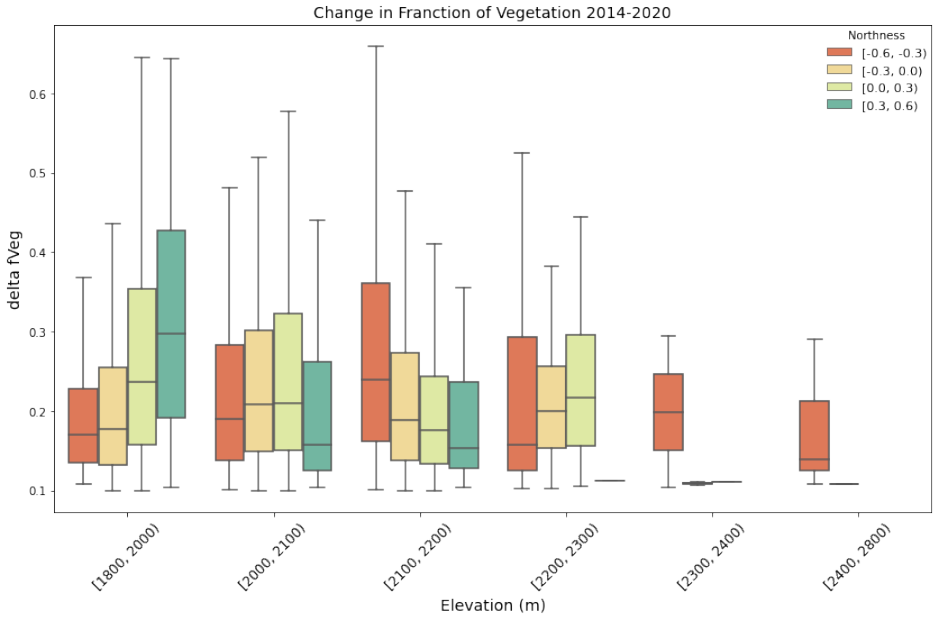

Figure A6. The spatial distribution of disturbance on the study domain. Disturbance increases with an increase in delta fVEG. Higher disturbance classes occur at lower elevations on both north-and south-facing slopes.

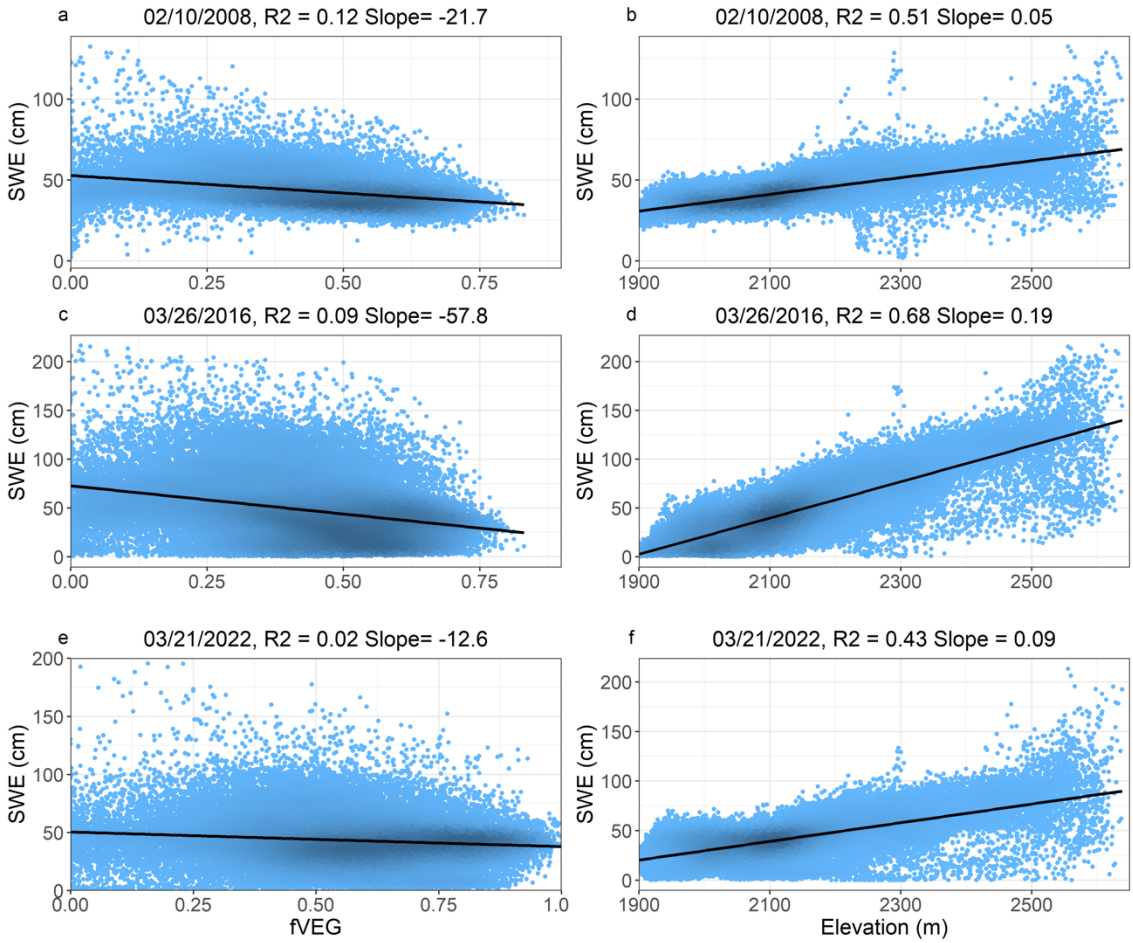

Figure A7. Linear regression results of terrain variables at the grid-scale including elevation and fraction of vegetation (fVEG) and snow water equivalent (SWE).

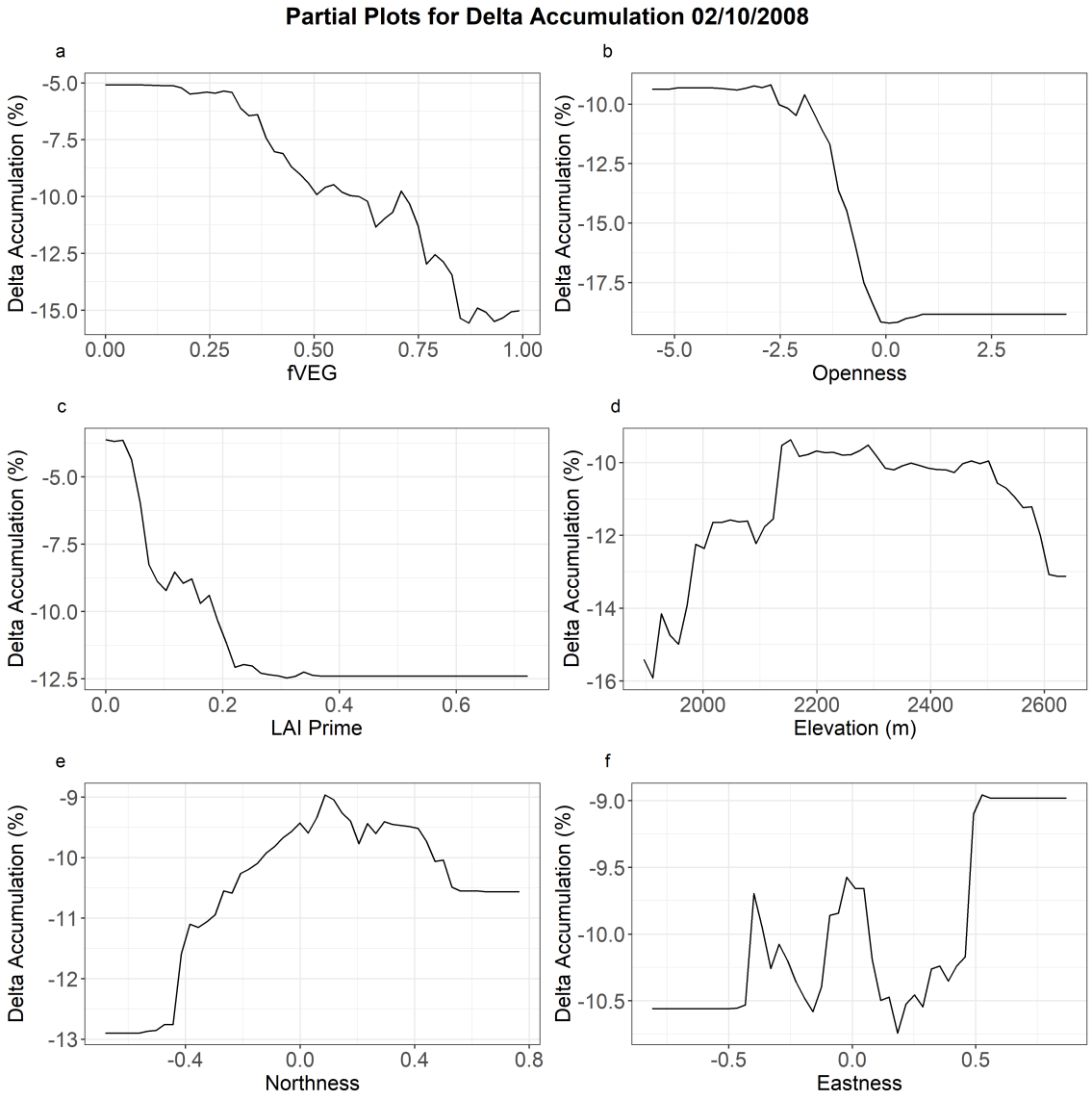

Figure A8. Partial plots for the delta accumulation space-for-structure RF model for the 02/10/2008 lidar flight.

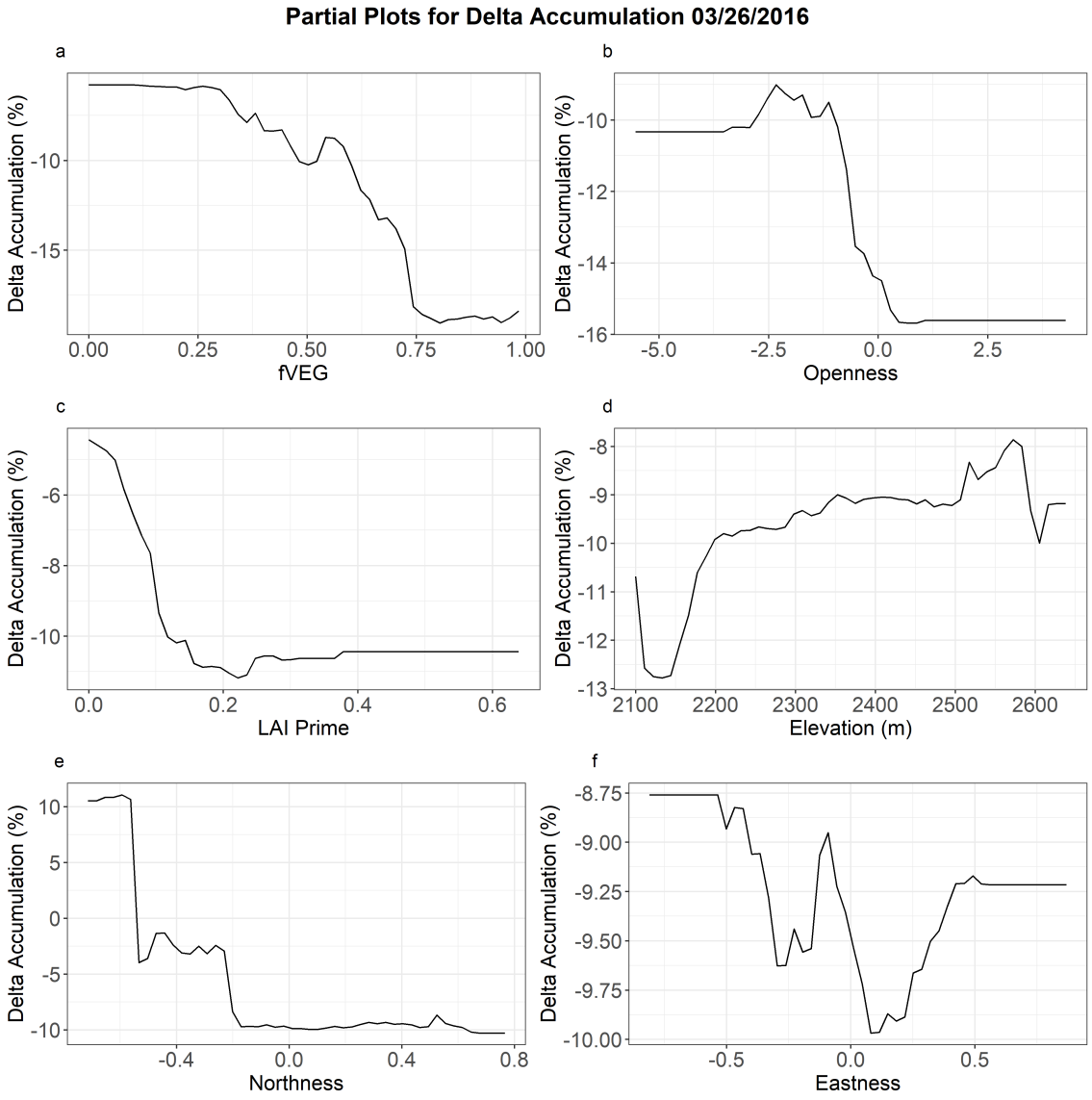

Figure A9. Partial plots for the delta accumulation space-for-structure RF model for the 03/26/2016 lidar flight.

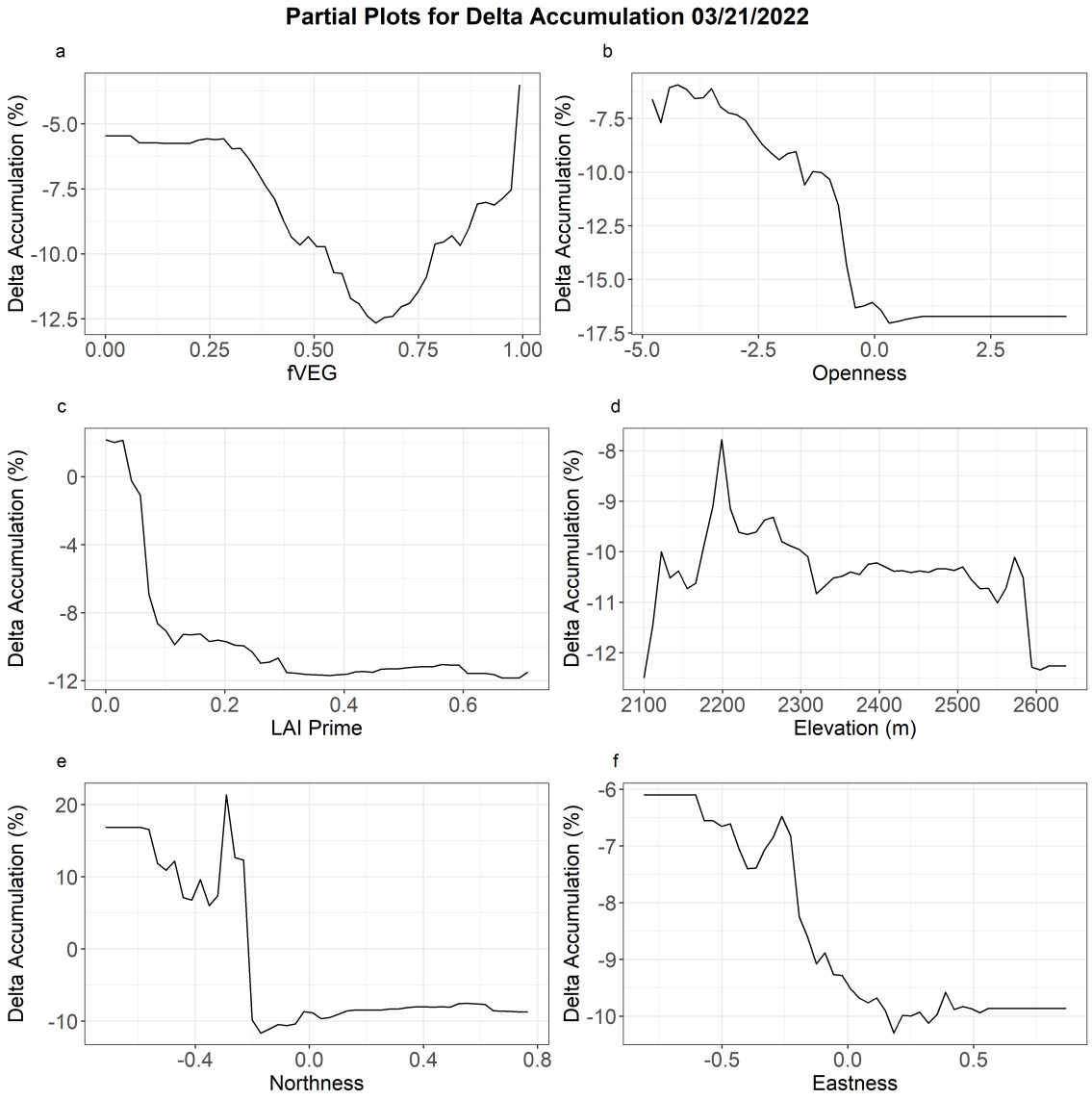

Figure A10. Partial plots for the delta accumulation space-for-structure RF model for the 03/21/2022 lidar flight.

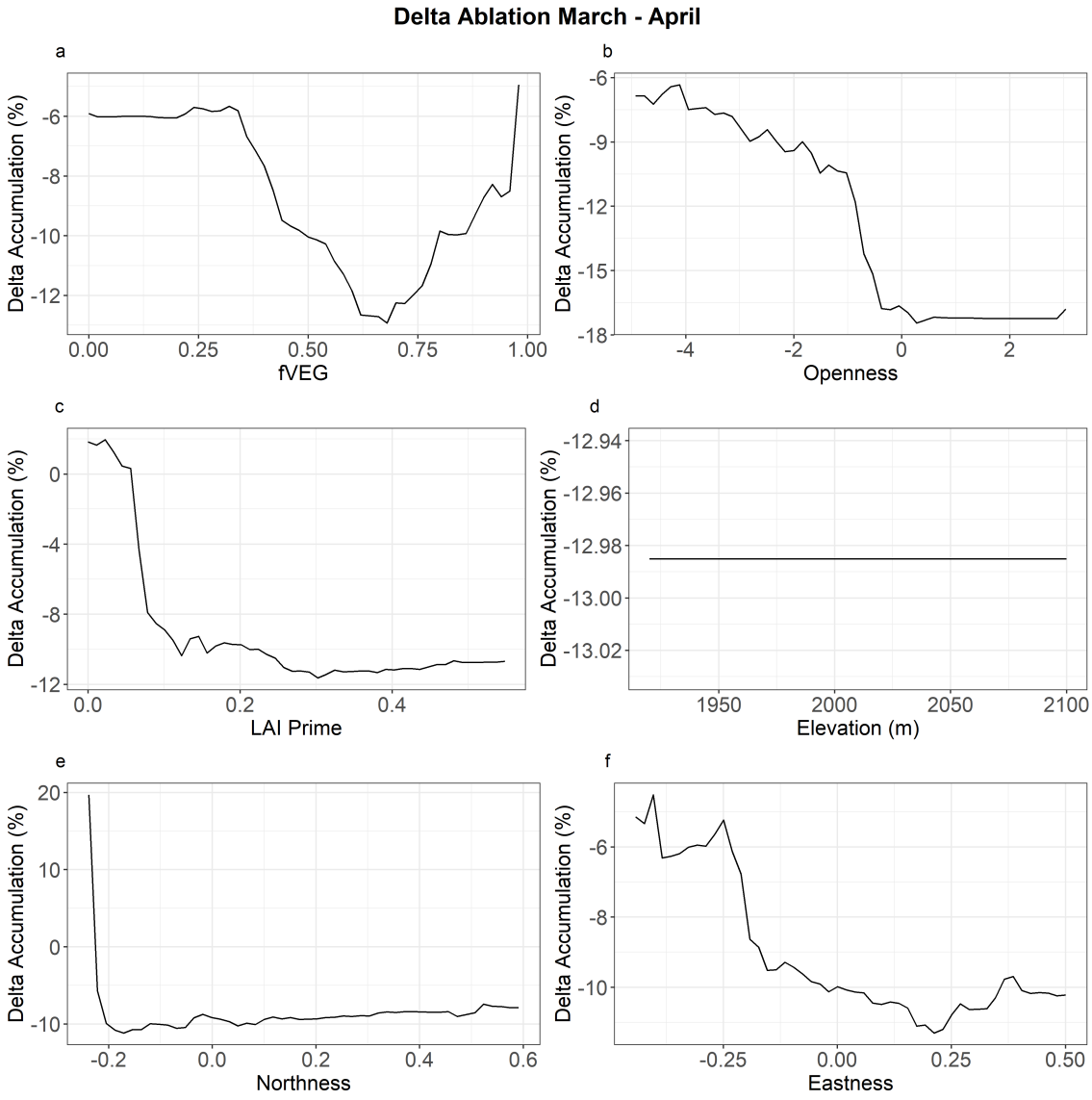

Figure A11. Partial plots for the normalize delta ablation space-for-structure RF model for the early season (March-April) analysis.

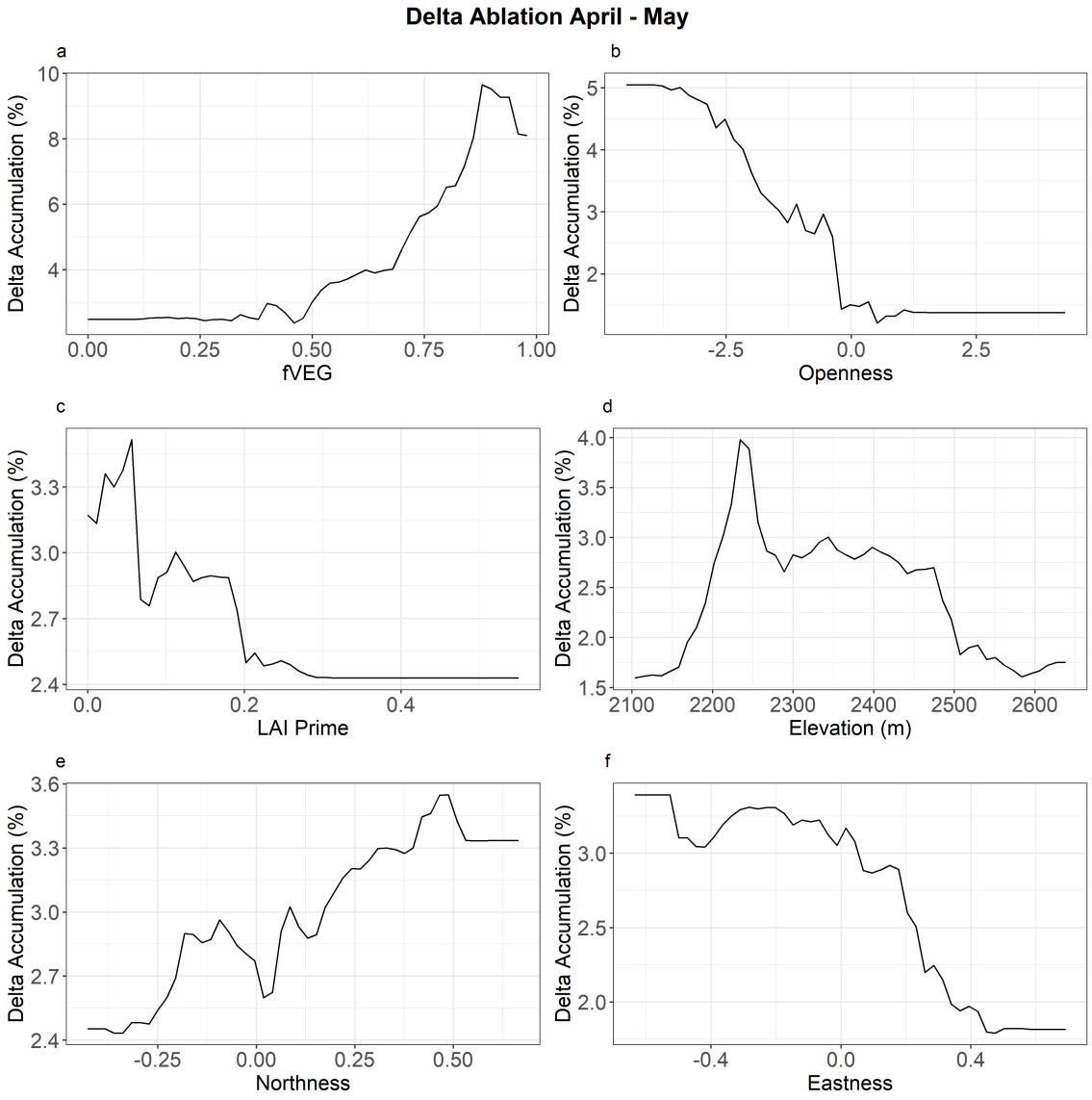

Figure A12. Partial plots for the normalize delta ablation space-for-structure RF model for the early season (April-May) analysis.

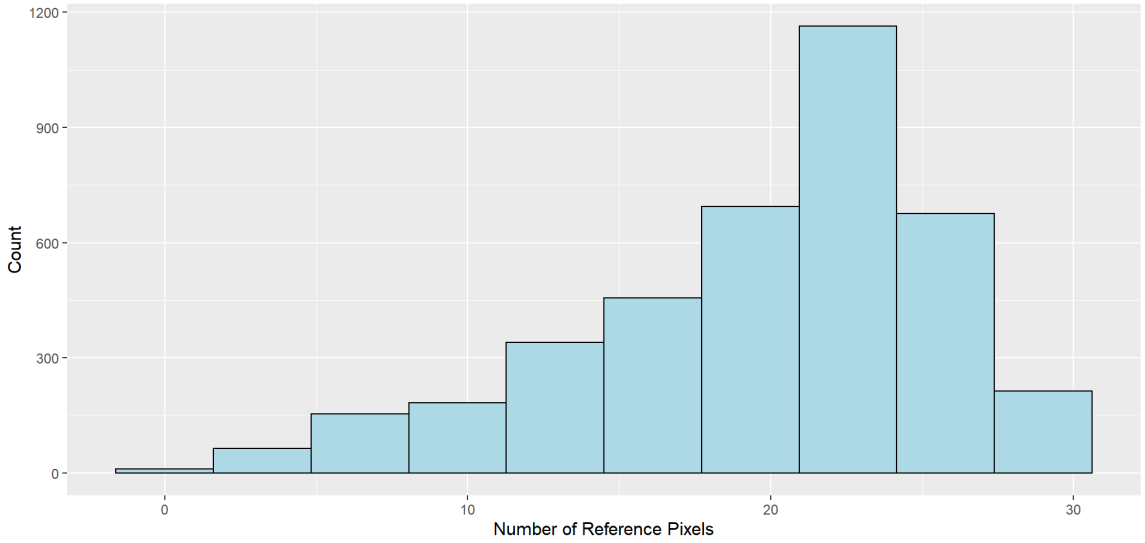

Figure A13. Reference pixel count using the search algorithm approach showing that most disturbed pixels had at least one reference pixel, up to a maximum of 30.

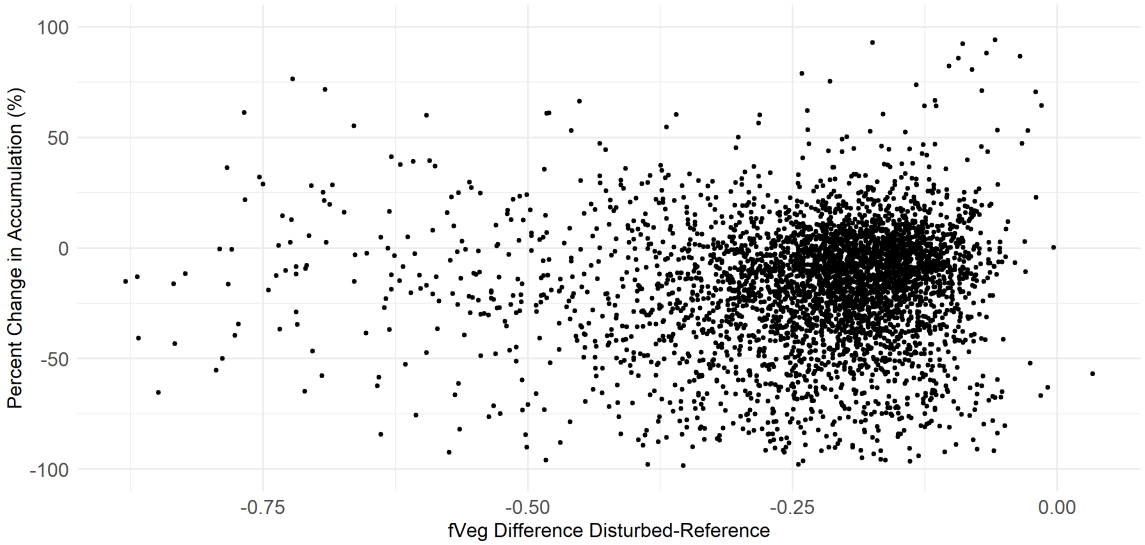

Figure A14. Results from the search algorithm displaying unclear relationships between the disturbed and reference pixels as fVEG increases in the disturbed pixel.

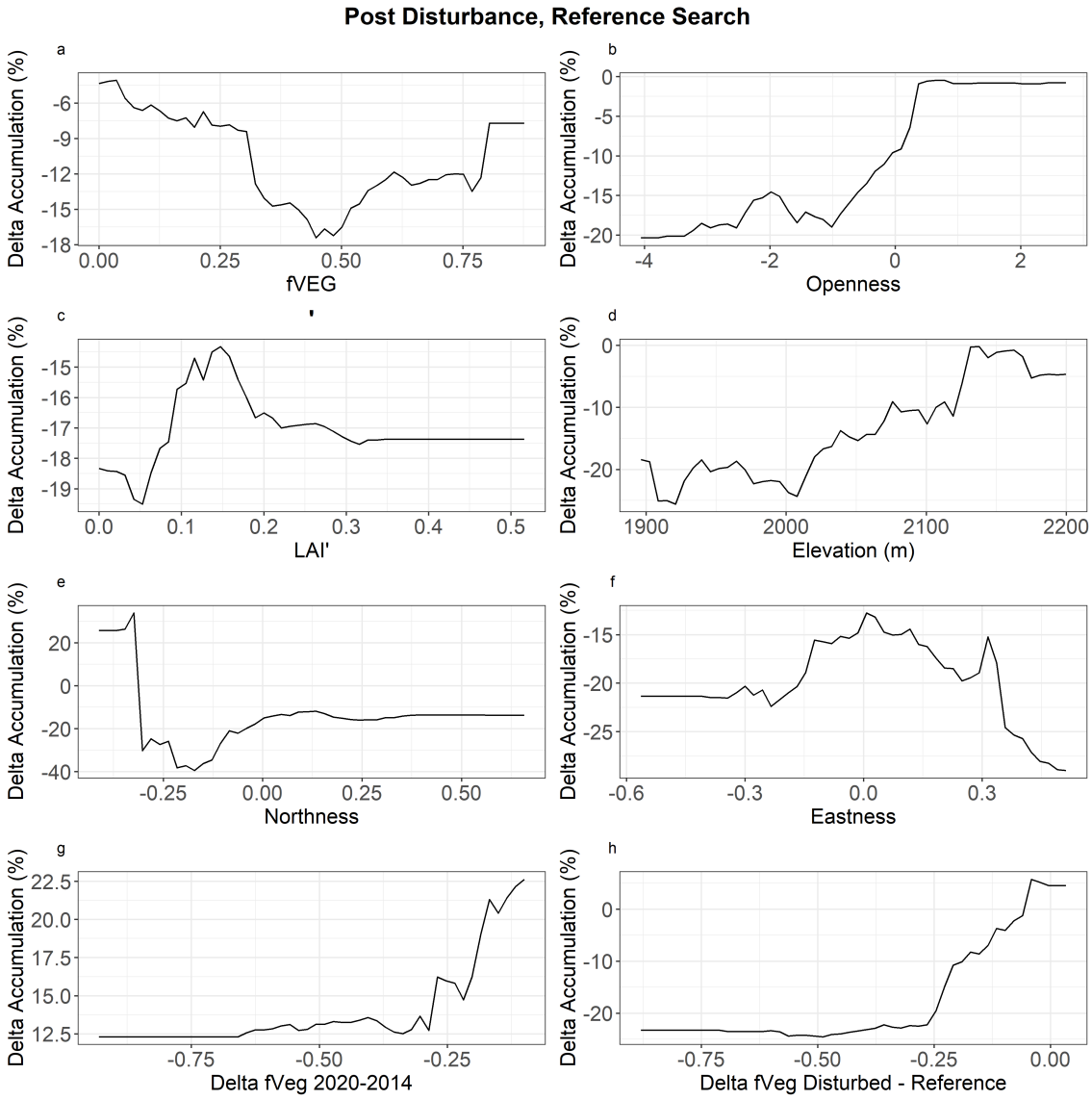

Figure A15. Partial plots for the normalize delta accumulation pre- and post-disturbance RF model using the search algorithm analysis.

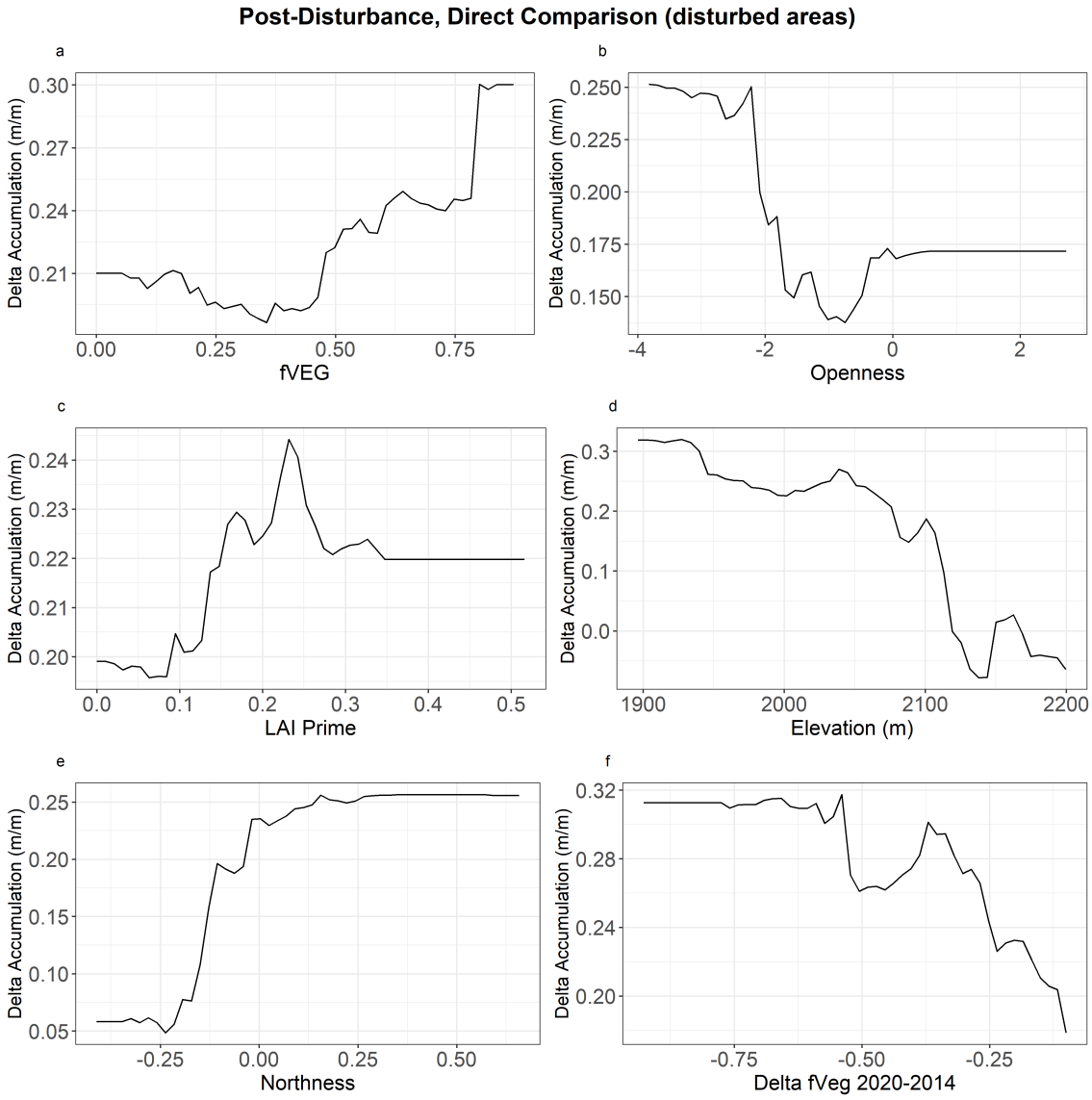

Figure A16. Partial plots for the normalize delta accumulation pre- and post-disturbance RF model using the direct comparison analysis (only disturbed areas).

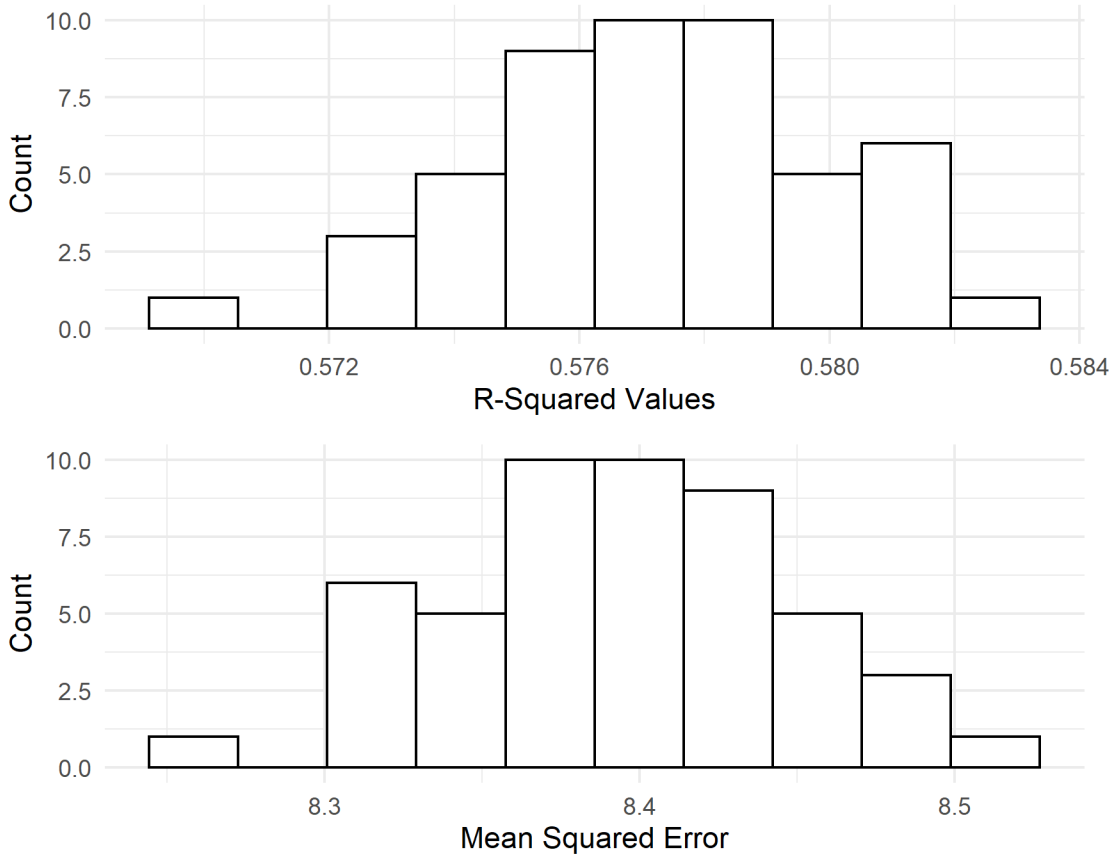

Figure A17. Example sensitivity analysis of the space-for-structure RF model predicting delta accumulation on 02/10/2008.